ELSEVIER

On the linear stability of plane Couette flow for an Oldroyd-B fluid and its numerical approximation

Raz Kupferman

Institute of Mathematics, The Hebrew University, Jerusalem, 91904, Israel

Abstract

It is well known that plane Couette flow for an Oldroyd-B fluid is linearly stable, yet, most numerical methods predict spurious instabilities at sufficiently high Weissenberg number. In this paper we examine the reasons which cause this qualitative discrepancy. We identify a family of distribution-valued eigenfunctions, which have been overlooked by previous analyses. These singular eigenfunctions span a family of non-modal stress perturbations which are divergence-free, and therefore do not couple back into the velocity field. Although these perturbations decay eventually, they exhibit transient amplification during which their "passive" transport by shearing streamlines generates large cross-stream gradients. This filamentation process produces numerical under-resolution, accompanied with a growth of truncation errors. We believe that the unphysical behavior has to be addressed by fine-scale modelling, such as artificial stress diffusivity, or other non-local couplings.
© 2005 Elsevier B.V. All rights reserved.

Keywords: Couette flow; Oldroyd-B model; Linear stability; Generalized functions; Non-normal operators; Stress diffusion

1. Introduction

The linear stability of Couette flow for viscoelastic fluids is a classical problem whose study originated with the pioneering work of Gorodtsov and Leonov (GL) back in the 1960s [1]; this problem has been further elaborated and generalized to various situations, such as Poiseuille and multi-layered flows, and applied to different constitutive laws; see [2–7]. The aforementioned work is based on spectral analysis. For Couette flow, the eigenvalues of the linearized perturbation equation are always on the left half of the complex plane, i.e., the corresponding eigenmodes decay in time. For infinite-dimensional non-normal operators, spectral analysis does not guarantee stability. Renardy [8] proved rigorously, however, that Couette flow for an upper-convected Maxwell (UCM) fluid is indeed linearly stable.

Although Couette flow is believed to be linearly stable under quite general conditions, numerical simulations often fail to predict stable behavior at sufficiently high Weissenberg number. This discrepancy between analysis and computations has attracted much attention. Numerical studies can be

divided into two main groups: (i) numerical solutions of the boundary value problem defined by the linearized system (e.g. [2,3]) and (ii) stability analysis of numerical methods for time-dependent flows, with the objective of understanding how spurious solutions emerge in computations. (e.g. [9–11]). A more recent benchmark study which compares the performance of various schemes in this context may be found in [12,13]. It is important to emphasize that the emergence of spurious instabilities is a purely linear phenomenon, but it is precisely this "simplicity" which makes it intriguing.

For concreteness, we will refer from now on to Couette flow of an Oldroyd-B fluid, although most of our analysis applies to a larger range of fluids. The linear partial differential equation that governs the evolution of small perturbations has two important characteristics: its spectrum has both discrete and continuous components, the latter corresponding to singular eigenfunctions, and it is highly non-normal, which in particular implies that small errors may significantly modify its spectrum. It is common to attribute the emergence of unstable modes to the failure of numerical methods to properly approximate the singular eigenfunctions. While this is (tautologically) correct, it yet does not explain the *mechanism* that leads to instabilities. The goal of this paper is to clarify

E-mail address: raz@math.huji.ac.il (R. Kupferman).

why numerical computations predict the wrong behavior, and propose ways to eliminate spurious instabilities.

In the first part of this paper we revisit the linear stability analysis for Couette flow for an Oldroyd-B fluid. While the spectrum itself has been known for long, controversies have remained regarding the precise nature of the singular eigenfunctions [3,4]. This question is fully elucidated by deriving analytical expressions for the singular eigenmodes; in particular, we find a family of distribution-valued eigenfunctions for the stress, consisting of delta functions and their derivatives, which are divergence-free, and therefore do not perturb the velocity field. As a consequence, these perturbations are *exact solutions of the full nonlinear system*. Furthermore, these singular eigenmodes form a basis for the construction of a large class of classical (non-modal) solutions, which are all decoupled from the velocity field. Such solutions are capable to sustain arbitrarily large stress gradients, which is indicative of the local nature of the constitutive laws.

We proceed with a numerical analysis in which we compare two finite-difference schemes. The first scheme, which uses naive central differencing, exhibits the standard scenario, where the straight lines of continuous spectra break into oval-shaped structures, and unstable modes emerge at a Weissenberg number around 10. In comparison, we construct a scheme that uses staggered vector and tensor fields [14]. This scheme is found to predict the correct spectrum with unprecedented accuracy. A closer examination reveals that this unexpected success is due the ability of the scheme to represent approximations (in the sense of distributions) of delta functions and their derivatives. If the problem is however changed, say, into Poiseuille flow, where the nature of the singularities is different, then the staggered scheme seems to offer no benefits over the central-difference scheme.

We then analyze the non-normal aspects of the perturbation equation, through the calculation of its pseudo-spectrum. Roughly speaking, the pseudo-spectrum provides a measure for how sensitive is the spectrum to a perturbation of the equations (for example, due to truncation errors). In addition, one may infer from the structure of the pseudo-spectrum estimates on the magnitude of the transient growth. As expected, the higher the Weissenberg number is, the smaller are the perturbations that may drive the system unstable, and the larger is the magnitude of the transient growth. Yet, this still does not explain what causes instabilities. Moreover, in many cases, unstable modes become dominant long after the transient growth has been attenuated [12]. An examination of the most amplified solution, which can be determined from a singular value decomposition, reveals that the long time behavior is dominated by solutions that belong to the family of divergence-free stress fields described above. Although these solutions decay in time, they develop in the transient a highly oscillatory profile, which for high enough Weissenberg number (i.e., long transient), quickly leads to cross-stream under-resolution. Large gradients that are aligned with the stream are usually damped out by the advection scheme, which has a dissipative component. This is not the case, however, with

cross-stream gradients. Thus, when the stress field oscillates in the cross-stream direction on the scale of a single computational cell, there is no damping mechanism, and one is left "at the mercy" of truncation errors, whose nature depends on the scheme chosen. We claim that it is the inability of numerical schemes to cope with such sub-grid variations which causes the emergence of spurious modes.

A fundamental question now arises: constitutive laws such as Oldroyd-B, UCM and other do not account for a non-local self-interaction of the stress field, and as a result, the stress in two neighboring stream lines evolves independently (in Lagrangian coordinates the stress satisfies an ordinary differential equation). In reality, the stress field experiences a small amount of diffusivity due to the random motion of the polymers center of mass; the dimensionless diffusivity coefficient is of the order of 10^{-9} [15], which makes it negligible on the scales imposed by numerical computations. Stress diffusion would precisely attenuate large cross-stream gradients, but in order to affect numerical computations the diffusivity coefficient should be about four orders of magnitude larger [16]. Is one allowed to introduce an artificially large diffusivity without significantly modifying the results?

The idea that sub-grid scales may be generated by advection and the use of stress diffusion to dampen those out are not new, and go back to the theoretical study of El-Kareh and Leal [15] (where it is even speculated that the coupled momentum-stress equations may be ill-posed without some amount of diffusivity), and the numerical study of Sureshkumar and Beris [16]. The use of artificial diffusion is now quite standard in the computation of turbulent viscoelastic flows, where the deformation of flow lines is extreme (see e.g. [17]). As usual, the concern is that the addition of diffusion will result in severe inaccuracy. It should be noted, however, that streamwise diffusion is built-in in any stable advection scheme. Yet, if the diffusivity coefficients scale with the square of the mesh size, second-order convergence can be guaranteed, at least in regions where the solution is sufficiently smooth. The "high-resolution" nature of the computation has to be established eventually via numerical convergence tests based on mesh refinement. Our opinion is that the same considerations should apply for cross-stream oscillations. One cannot just "ignore" sub-grid oscillations; they should either be damped, in order to maintain smoothness on the scale of a single cell, and if this introduces too large errors, sub-grid modelling is necessary. Since the physics do account for some diffusivity, although on a finer scale, the introduction of artificial diffusivity seems to be a natural solution. In either case, validation via mesh refinement is necessary.

2. Spectral analysis of Couette flow

2.1. Summary of known results

We consider an Oldroyd-B fluid in a two-dimensional channel, $x \in \mathbb{R}$, $y \in [-1/2, 1/2]$. In a creeping flow regime

(inertial terms are negligible), the governing equations are

$$-\nabla p + \lambda^{-1}(1-\beta)\,\nabla\cdot\boldsymbol{\sigma} + \beta\,\nabla^2\boldsymbol{u} = 0, \qquad \nabla\cdot\boldsymbol{u} = 0,$$

$$\frac{\partial\boldsymbol{\sigma}}{\partial t} + (\boldsymbol{u}\cdot\nabla)\boldsymbol{\sigma} - (\nabla\boldsymbol{u})\boldsymbol{\sigma} - \boldsymbol{\sigma}(\nabla\boldsymbol{u})^{\mathrm{T}} = \lambda^{-1}(\boldsymbol{I}-\boldsymbol{\sigma}), \qquad (2.1)$$

where $\boldsymbol{u} = (u, v)$ is the velocity, $\boldsymbol{\sigma}$ the conformation tensor, with components σ^{ij}, p the pressure, β the Newtonian to total viscosity ratio, and λ the polymeric relaxation time, which in our dimensionless setting coincides with the Weissenberg number. The velocity gradient tensor has entries $(\nabla\boldsymbol{u})_{ij} = \partial u_i/\partial x_j$. The shear-flow boundary conditions are $\boldsymbol{u} = (\pm 1/2, 0)$ at $y = \pm 1/2$.

Normalized Couette flow corresponds to the stationary solution:

$$\boldsymbol{u} = (y, 0) \equiv \boldsymbol{U} \qquad \text{and} \qquad \boldsymbol{\sigma} = \begin{pmatrix} 1+2\lambda^2 & \lambda \\ \lambda & 1 \end{pmatrix} \equiv \boldsymbol{\Sigma}.$$

Adopting the standard practice, we write the solution to (2.1) as a sum of the steady solution and a perturbation,

$$\boldsymbol{u}(x, y, t) = \boldsymbol{U} + \delta\boldsymbol{u}(x, y, t), \qquad p(x, y, t) = \delta p(x, y, t),$$

$$\boldsymbol{\sigma}(x, y, t) = \boldsymbol{\Sigma} + \delta\boldsymbol{\sigma}(x, y, t).$$

Linearizing (2.1) with respect to the functions $\delta\boldsymbol{u}$, δp and $\delta\boldsymbol{\sigma}$, we obtain the perturbed system:

$$-\nabla\delta p + \lambda^{-1}(1-\beta)\,\nabla\cdot\delta\boldsymbol{\sigma} + \beta\,\nabla^2\delta\boldsymbol{u} = 0, \qquad \nabla\cdot\delta\boldsymbol{u} = 0,$$

$$\left(\frac{\partial}{\partial t} + \frac{1}{\lambda} + y\,\frac{\partial}{\partial x}\right)\delta\boldsymbol{\sigma} = [(\nabla\delta\boldsymbol{u})\boldsymbol{\Sigma} + \boldsymbol{\Sigma}(\nabla\delta\boldsymbol{u})^{\mathrm{T}}]$$

$$+ [(\nabla\boldsymbol{U})\delta\boldsymbol{\sigma} + \delta\boldsymbol{\sigma}(\nabla\boldsymbol{U})^{\mathrm{T}}], \qquad (2.2)$$

which governs the evolution of small perturbations about plane Couette flow. The boundary conditions are imposed by the no-slip conditions: $\delta\boldsymbol{u} = (0, 0)$ at $y = \pm 1/2$.

The structure of the problem merits some comment: the dynamical variables are the three components of the conformation tensor $\boldsymbol{\sigma}$—the system (2.1) prescribes the rate of change of $\boldsymbol{\sigma}$ given its current state. The velocity and the pressure are "slaved" to the conformation tensor via the elliptic Stokes equations, which can also be interpreted in terms of a constrained optimization problem: the velocity $\boldsymbol{u}$ minimizes the Frobenius norm:

$$\|\lambda^{-1}(1-\beta)\,\boldsymbol{\sigma} - \tfrac{1}{2}\beta(\nabla\boldsymbol{u} + \nabla\boldsymbol{u}^{\mathrm{T}})\|_F, \qquad (2.3)$$

subject to the incompressibility constraint $\nabla\cdot\boldsymbol{u} = 0$. Thus, the perturbation in the velocity $\delta\boldsymbol{u}$ depends linearly (but non-locally) on the perturbation in the conformation tensor, $\delta\boldsymbol{\sigma}$, which implies that (2.2) can be recast in the general form

$$\frac{\partial}{\partial t}\delta\boldsymbol{\sigma} = A\,\delta\boldsymbol{\sigma},$$

where A is a linear integro–differential operator. (For a UCM fluid the momentum equation acts as a constraint on the evo-

lution of the stress, and an anisotropic Stokes-like problem may be obtained via the so-called EEME formulation [18]).

Since the system (2.2) does not depend explicitly on the coordinate x, it is natural to Fourier expand the perturbation along this coordinate. Spectral analysis consists of looking for solutions of the form

$$\delta\boldsymbol{u}(x, y, t) = \delta\boldsymbol{u}(y)\,\mathrm{e}^{\mathrm{i}kx+\omega t}, \qquad \delta p(x, y, t) = \delta p(y)\,\mathrm{e}^{\mathrm{i}kx+\omega t},$$

$$\delta\boldsymbol{\sigma}(x, y, t) = \delta\boldsymbol{\sigma}(y)\,\mathrm{e}^{\mathrm{i}kx+\omega t},$$

which substituted into (2.2) yield

$$-\nabla\delta p + \lambda^{-1}(1-\beta)\,\nabla\cdot\delta\boldsymbol{\sigma} + \beta\,\nabla^2\delta\boldsymbol{u} = 0, \qquad \nabla\cdot\delta\boldsymbol{u} = 0,$$

$$\left(\omega + \frac{1}{\lambda} + \mathrm{i}ky\right)\delta\boldsymbol{\sigma} = [(\nabla\delta\boldsymbol{u})\boldsymbol{\Sigma} + \boldsymbol{\Sigma}(\nabla\delta\boldsymbol{u})^{\mathrm{T}}]$$

$$+ [(\nabla\boldsymbol{U})\delta\boldsymbol{\sigma} + \delta\boldsymbol{\sigma}(\nabla\boldsymbol{U})^{\mathrm{T}}]. \qquad (2.4)$$

Here derivation with respect to x should be interpreted as a multiplication by $\mathrm{i}k$.

For every axial wavenumber k, the linear system (2.4) is a one-dimensional boundary value problem. Its *spectrum* is the set of ω for which the system has a non-trivial solution $\delta\boldsymbol{\sigma}$. It is possible, following [1], to reduce (2.4) into a scalar fourth-order equation for the stream function. The drawback of this reduction is that the structure of the problem is thus changed. As was emphasized above, the dynamical variables are the components of the conformation tensor and not the velocity, nor the stream function. In particular, the boundary value problem (2.4) may have non-trivial solutions *for which the perturbed velocity vanishes*. Such eigenfunctions would be trivial solutions of the fourth-order scalar equation, but are not trivial solutions of (2.4). As will be seen in Section 2.2, this delicacy has been the source of a certain confusion in the past.

The spectrum for a UCM fluid, i.e., for the system (2.1) with $\beta = 0$, was fully characterized by Gorodtsov and Leonov [1]. It consists of two discrete eigenvalues – the *discrete* GL *eigenvalues* – which can be computed analytically, and a continuous strip of eigenvalues, $\omega = -1/\lambda - \mathrm{i}ky_0$, $y_0 \in [-1/2, 1/2]$ – the continuous, or *singular GL eigenvalues*. The real part of the two discrete eigenvalues approaches the value $-1/2\lambda$ for $\lambda \gg 1$; in the opposite limit, $\lambda \ll 1$, they tend towards the continuous GL strip of eigenvalues. The spectrum for an Oldroyd-B fluid contains an additional continuous strip $\omega = -1/\beta\lambda - \mathrm{i}ky_0$, $y_0 \in [-1/2, 1/2]$ – the continuous, or *singular "viscous" eigenvalues* – and a finite number of discrete eigenvalues – the *discrete "viscous" eigenvalues* – the number of which tends to infinity in the singular limit $\beta \to 0$; see Wilson et al. [6] for details.

While the spectrum of this system is well-established, there have been some controversies regarding the nature of the eigenfunctions. The eigenfunctions associated with the discrete eigenvalues are known to be smooth and spatially extended. In contrast, the eigenfunctions associated with the singular spectra are known to be singular. Sureshkumar and Beris [3] suggested that the singular eigenfunctions were in

fact not functions, but generalized functions, or distributions. This possibility was ruled out by Graham [4], who, for a UCM fluid, obtained analytical expressions for eigenfunctions that are continuously differentiable, i.e., their non-analyticity only reflects in the second derivative. The analysis below will show that distribution-valued eigenfunctions do exist *in addition* to those discovered by Graham.

For linear finite-dimensional systems, that is, systems of the form $\partial u/\partial t = Au$, where A is a matrix, and for infinite-dimensional systems where A is a normal operator (it commutes with its adjoint), the solution is stable if and only if the spectrum of A lies in the left half of the complex plane. This condition does not guarantee stability for operators A that are non-normal. The implications of non-normality may be much more dramatic than just the fact that "transient growth may occur"; we will return to this point in Section 4. It is however important to emphasize that the stability of Couette flow cannot be deduced solely from an examination of its spectrum. A rigorous stability proof for a UCM fluid, based on Sobolev norm estimates, is given in Renardy [8].

2.2. The singular GL eigenfunctions

As mentioned above, the nature of the singular GL eigenfunctions has been debated in [3,4]. In [4] continuously differentiable eigenfunctions that correspond to the strip of eigenvalues $\omega = -1/\lambda - iky_0$, $y \in [-1/2, 1/2]$, were constructed for a UCM fluid. In fact, two linearly independent eigenfunctions exist for every eigenvalue along this strip. For an Oldroyd-B fluid, the degeneracy is removed, and a single family of "Graham-type" eigenfunctions exists for this range of eigenvalues.

A central result in the present work is the discovery of a new family of eigenfunctions, $\delta\boldsymbol{\sigma}_{y_0}(y)$, $y_0 \in [-1/2, 1/2]$, corresponding to the eigenvalues $\omega = -1/\lambda - iky_0$. These eigenfunctions are generalized functions, or distributions, given by

$$\delta\boldsymbol{\sigma}_{y_0}(y) = \begin{pmatrix} -\delta''_{y_0}(y) & ik\,\delta'_{y_0}(y) \\ ik\,\delta'_{y_0}(y) & k^2\,\delta_{y_0}(y) \end{pmatrix}. \tag{2.5}$$

Here δ_{y_0} is the Dirac distribution concentrated at the point y_0, defined by its action on test function: $(\delta_{y_0}, \phi) = \phi(y_0)$; its j-th (weak) derivative, $\delta^{(j)}_{y_0}$ is defined by $(\delta^{(j)}_{y_0}, \phi) = (-1)^j \phi^{(j)}(y_0)$. A straightforward substitution shows that (2.5) does indeed solve (2.4), in a distributional sense, with $\omega = -1/\lambda - iky_0$. To verify that, one needs to multiply (2.4) by a test function $\phi \in C_0^\infty([-1/2, 1/2])$, integrate over $y \in [-1/2, 1/2]$, formally integrate by parts such to transfer all derivatives onto the smooth function ϕ, and verify that the resulting expression is valid for any test function.[1]

The occurrence of distribution-valued eigenfunctions is by itself not disturbing. Consider the much simpler problem of a Schrödinger equation for a free particle on the line:

$$i\hbar\frac{\partial\psi}{\partial t} = -\frac{\hbar^2}{2m}\nabla^2\psi.$$

The spectrum of this equation covers the entire real line, and the eigenfunction that corresponds to the eigenvalue $\omega = -i\hbar k^2/2m$ is e^{ikx}. While this eigenfunction is infinitely differentiable, it does not belong to the space $L^2(\mathbb{R})$ in which the problem is defined, and as such is not "better" than a delta distribution. In fact, the correct interpretation of these eigenfunctions is as distributions in $\mathbb{R}$ (see von Neumann [20] for a discussion of these and related issues). Nevertheless, these distributions are building blocks for generating functions that do reside within $L^2(\mathbb{R})$.[2]

The generalized eigenfunctions (2.5) have the property that their divergence (interpreted in the sense of distributions) vanishes identically. Thus, the corresponding velocity perturbation $\delta\boldsymbol{u}$ is zero. Since the only non-linearity in (2.1) is due to quadratic terms that involve multiplication of the velocity and the conformation tensor, it follows that any tensor-valued distribution of the form

$$\boldsymbol{\sigma}(x, y, t) = \boldsymbol{\Sigma} + \sum_{k, y_0} a_{k, y_0}\,\delta\boldsymbol{\sigma}_{y_0}(y)\,e^{-(t/\lambda)+ik(x-y_0 t)},$$

with $\delta\boldsymbol{\sigma}_{y_0}(y)$ given by (2.5), is a solution (in the sense of distributions) of *the full nonlinear system* (2.1), with $\boldsymbol{u} = U$. This family of solutions, parameterized by the sets of coefficients a_{k, y_0} is by itself unphysical, but it constitutes a building block for a large class of solutions.

Indeed, replace a_{k, y_0} by a three-time differentiable function, $\hat{\phi}_k(y_0)$, where for every y_0, $\hat{\phi}_k(y_0)$ is the Fourier transform of a three-time differentiable function $\phi(x, y_0)$. Integrate over both k and y_0, to obtain, after simple manipulations, a family of *classical* solution of the form

$$\boldsymbol{\sigma}(x, y, t) = \boldsymbol{\Sigma} + e^{-t/\lambda}\begin{pmatrix} -\partial_{yy}^2 & \partial_{xy}^2 \\ \partial_{xy}^2 & -\partial_{xx}^2 \end{pmatrix}\phi(x - yt, y). \tag{2.6}$$

The function ϕ is known in the literature as an *Airy stress function*; it is first evaluated at the point $(x - yt, y)$, and only then differentiated with respect to x and y. Eq. (2.6) can also be written in the alternative form:

---

[1] We remind the reader that a distribution u in a space X is a linear form on the space of test functions $C_0^\infty(X)$, such that for every compact subset $K \subset X$ there exist constants k, c, such that $|(u, \phi)| \le c\sum_{|\alpha| \le k}\sup_K|\partial_\alpha\phi|$, for all $\phi \in C_0^\infty(K)$. This space is denoted by $\mathscr{D}'(X)$. The subset of distributions for which the same k can be used for all compact K is called the space of distributions of order k and it is denoted by $\mathscr{D}'^k(X)$. Thus, $\delta\boldsymbol{\sigma}_{y_0}$ defined by (2.5) belongs to the space of second-rank tensor-valued distributions of order two in $[-1/2, 1/2]$, since it involves at most a second derivative of the delta distribution. See Gel'fand and Shilov [19] for a classical reference on generalized functions.

[2] A Hilbert space, for example $L^2(\mathbb{R})$, together with a subspace which carries a finer topology, such as the set of test functions in $\mathbb{R}$, is called a *rigged Hilbert space*. This construction allows to link between distributions and square-integrable aspects of functional analysis to formalize spectral analysis.

$$\delta\boldsymbol{\sigma}(x, y, t) = \mathrm{e}^{-t/\lambda}\left[\begin{pmatrix} -\phi_{yy} & \phi_{xy} \\ \phi_{xy} & -\phi_{xx} \end{pmatrix} + t\begin{pmatrix} 2\phi_{xy} & -\phi_{xx} \\ -\phi_{xx} & 0 \end{pmatrix}\right.$$
$$\left. + t^2\begin{pmatrix} -\phi_{xx} & 0 \\ 0 & 0 \end{pmatrix}\right], \tag{2.7}$$

where the partial derivatives of ϕ are evaluated at the point $(x - yt, y)$.

The existence of solutions of the form (2.7) can be derived directly, without reference to spectral analysis. Let $\boldsymbol{f} = \nabla \cdot \delta\boldsymbol{\sigma}$ (a vector proportional to the perturbation in the polymeric forces), then its components (f_x, f_y) satisfy the system of equations

$$\left(\frac{\partial}{\partial t} + \frac{1}{\lambda} + y\frac{\partial}{\partial x}\right)f_x = f_y + (1 + 2\lambda^2)\frac{\partial^2 \delta u}{\partial x^2}$$
$$+ 2\lambda\frac{\partial^2 \delta u}{\partial x \partial y} + \frac{\partial^2 \delta u}{\partial y^2} \tag{2.8a}$$

$$\left(\frac{\partial}{\partial t} + \frac{1}{\lambda} + y\frac{\partial}{\partial x}\right)f_y = (1 + 2\lambda^2)\frac{\partial^2 \delta v}{\partial x^2} + 2\lambda\frac{\partial^2 \delta v}{\partial x \partial y} + \frac{\partial^2 \delta v}{\partial y^2}. \tag{2.8b}$$

Since $\boldsymbol{f} = 0$ (no forcing) implies $u = v = 0$, it follows from (2.8) that the space of divergence-free perturbations $\delta\boldsymbol{\sigma}$ is invariant under the linearized dynamics (2.2). Every $\delta\boldsymbol{\sigma}(x, y, t)$ in this invariant subspace can be represented as

$$\delta\boldsymbol{\sigma}(x, y, t) = \begin{pmatrix} -\dfrac{\partial^2 \Phi}{\partial y^2}(x, y, t) & \dfrac{\partial^2 \Phi}{\partial x \partial y}(x, y, t) \\ \dfrac{\partial^2 \Phi}{\partial x \partial y}(x, y, t) & -\dfrac{\partial^2 \Phi}{\partial x^2}(x, y, t) \end{pmatrix}.$$

Substituting into (2.2), we deduce that $\delta\boldsymbol{\sigma}(x, y, t)$ is of the form (2.7).

To conclude, Couette flow of an Oldroyd-B fluid allows for a class of divergence-free perturbations which do not perturb the velocity field. The initial perturbation, which is determined by the function $\phi(x, y)$ is advected with the flow, and decays as a result of the stress relaxation at a rate $1/\lambda$. The interesting feature is that there is no restriction on the shape of the perturbation, which can sustain arbitrarily large spatial gradients (as long as it is divergence-free). This reflects the fact that the only non-local interaction in the Oldroyd-B model is via the velocity field, thus the model reduces to a local equation (ODEs) in cases where the stress does not couple back into the velocity field.

2.3. The singular viscous eigenfunctions

The structure of the singular viscous eigenfunctions can be deduced from the analysis in Wilson et al. [6]; there are however certain points worth of further elaboration.

First, it follows from (2.8) that

$$\left(\frac{\partial}{\partial t} + \frac{1}{\lambda} + y\frac{\partial}{\partial x}\right)\nabla \cdot \boldsymbol{f} = 0,$$

which means that the space of perturbations for which $\nabla \cdot \nabla \cdot \delta\boldsymbol{\sigma} = 0$ is invariant under the linearized dynamics. It will be shown that the singular viscous eigenfunctions all lie within this invariant subspace.

The singular viscous spectrum lies on the segment $\omega = -1/\beta\lambda + \mathrm{i}ky_0$, $y_0 \in [-1/2, 1/2]$. From the property $\nabla \cdot \nabla \cdot \delta\boldsymbol{\sigma} = 0$, it follows that $\nabla^2 \delta p = 0$, hence $\delta p(y)$ is a linear combination of e^{ky} and e^{-ky}. Substituting into the momentum equation for δv, we get

$$\delta v'' - k^2 \delta v = -\mu f_y + c_1 \mathrm{e}^{ky} + c_2 \mathrm{e}^{-ky},$$

where $\mu = (1 - \beta)/(\beta\lambda)$, and c_1, c_2 are integration constants. Substituting this equation into (2.8b) with $\omega = -1/\beta\lambda + \mathrm{i}ky_0$, we find

$$(y - y_0)(\delta v'' - k^2 \delta v) + 2\mu\lambda \delta v' + 2\mathrm{i}k\mu\lambda^2 \delta v$$
$$= (-\mu + \mathrm{i}k(y - y_0))(c_1 \mathrm{e}^{ky} + c_2 \mathrm{e}^{-ky}),$$

where the constants $c_{1,2}$ have been redefined. It can be directly verified that functions of the form

$$\delta v(y) = \left(-\frac{1}{\beta\lambda} + \mathrm{i}k(y - y_0)\right)(c_1 \mathrm{e}^{ky} + c_2 \mathrm{e}^{-ky}) \tag{2.9}$$

are solutions of this inhomogeneous equation (with $c_{1,2}$ redefined again), so that the general solution is obtained by adding to (2.9) a linear combination of the two independent solutions of the homogeneous equation:

$$(y - y_0)(\delta v'' - k^2 \delta v) + 2\mu\lambda \delta v' + 2\mathrm{i}k\mu\lambda^2 \delta v = 0,$$

which are

$$\delta v(y) = \mathrm{e}^{-ky}[c_3 \,_1F_1(a, b, 2k(y - y_0))$$
$$+ c_4 U(a, b, 2k(y - y_0))],$$

where the functions $_1F_1$ and U are the confluent hypergeometric functions [21], and $a = \mu\lambda(1 - \mathrm{i}\lambda)$, $b = 2\mu\lambda$. While $_1F_1(a, b, z)$ is analytic in its three arguments, the function $U(a, b, z)$ has an algebraic singularity at $z = 0$ of the form $U(a, b, z) \sim z^{1-b}$.

The four integration constants c_1–c_4 should be determined, up to a proportionality factor, by the boundary conditions, $\delta v(\pm 1/2) = \delta v'(\pm 1/2) = 0$. A priori there is no reason why this linear system should have a non-trivial solution for every y_0. The existence of a solution stems from the singular nature of the equations, and consequently, the analysis extends as for the singular GL modes to the space of generalized functions.

A simple example that illustrates how do non-trivial distribution-valued solutions emerge is the following

second-order equation for $y(t)$ with homogeneous boundary conditions:

$$t\,y'' + \tfrac{5}{2}y' = 0, \qquad y(-1) = y(1) = 0. \tag{2.10}$$

Away from the singularity at $t = 0$, this equation has two independent solutions, $y = c$, and $y = t^{-3/2}$, however the latter is not summable at the origin, and is therefore not a valid distribution. Yet, the function $t^{-3/2}$ can be *regularized* giving rise to *two* independent distributions which satisfy (2.10). These two distributions, denoted by $t_+^{-3/2}$ and $t_-^{-3/2}$, are defined by their action on test functions ϕ,

$$(t_+^{-3/2}, \phi) = \int_0^1 \frac{\phi(t) - \phi(0)}{t^{3/2}}\,\mathrm{d}t,$$

$$(t_-^{-3/2}, \phi) = \int_{-1}^0 \frac{\phi(t) - \phi(0)}{t^{3/2}}\,\mathrm{d}t$$

(see Gel'fand and Shilov [19]). It can directly be verified that any distribution proportional to

$$y(t) = t_+^{-3/2} + t_-^{-3/2} - 1$$

is a solution of (2.10).

Similarly, the singular function $U(a, b, 2k(y - y_0))$ gives rise to two independent (regularized) distributions

$$(y - y_0)^{2\mu\lambda - 1}U(a, b, 2k(y - y_0))(y - y_0)_\pm^{1-2\mu\lambda}.$$

With now five constants of integration, non-trivial distribution-valued solutions $\delta v(y)$ can be found, which satisfy the four boundary conditions. By the nature of the regularization, the leading-order term in $\delta v(y)$ scales like the $\lfloor 2\mu\lambda - 1 \rfloor = \lfloor 1/\beta - 2 \rfloor$-th derivative of the delta distribution at y_0.

3. Analysis of finite-difference approximations

Although Couette flow for an Oldroyd-B fluid is stable, most numerical schemes predict the emergence of spurious unstable modes at sufficiently high Weissenberg number. In this section we compare the spectral properties of two finite-difference approximations for time dependent flows. The first scheme is based on standard finite-differences, and exhibits the known splitting of the continuous spectrum into oval structures, which, for high enough Weissenberg numbers protrude into the right half plane. The second scheme uses a staggered setting for the conformation tensor, and is found to predict the correct spectrum with very high accuracy. It will be shown that this success is somewhat "accidental", and the staggered setting does not appear to perform better in general situations.
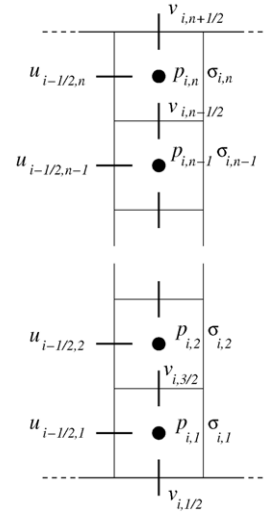

Fig. 1. Discrete geometry for the central difference scheme.

3.1. A central-difference scheme

We start by describing a standard central-difference scheme. The velocity field is discretized on a staggered (Marker-and-Cell) mesh [22]: velocity variables are defined at cell edges, with only the normal component defined at each edge. This staggered discretization is used for all vector fields, such as the pressure gradient and the divergence of the conformation tensor. The conformation tensor and the pressure are defined at cell centers. The geometry of the system is depicted in Fig. 1.

Let n be the number of computational cells across the channel, and $\Delta x = \Delta y = 1/n$ be the mesh size. Pressure and conformation tensor variables, which are cell-centered are denoted by $p_{i,j}$ and $\sigma_{i,j}$, respectively, $i \in \mathbb{Z}$, $j = 1, 2, \ldots, n$. The discrete velocity variables, which are edge-centered, are denoted by $u_{i\pm 1/2, j}$, and $v_{i, j\pm 1/2}$, the indexing being self-explanatory.

Given a configuration of the conformation tensor, we first calculate its divergence, which is a vector field (i.e., has a "velocity-like" representation):

$$\left(\frac{\partial \sigma^{xx}}{\partial x} + \frac{\partial \sigma^{xy}}{\partial y} \right)_{i+1/2, j} = D_x^+ \sigma_{i,j}^{xx} + \mu_x^+ D_y^0 \sigma_{i,j}^{xy},$$

$$\left(\frac{\partial \sigma^{xy}}{\partial x} + \frac{\partial \sigma^{yy}}{\partial y} \right)_{i, j+1/2} = \mu_y^+ D_x^0 \sigma_{i,j}^{xy} + D_y^+ \sigma_{i,j}^{yy}, \tag{3.1}$$

where $D_{x,y}^+$, $D_{x,y}^-$, and $D_{x,y}^0$ are the standard forward-, backward-, and central-difference operators along the x and y directions; $\mu_{x,y}^\pm$ are forward- and backward-averaging operators along the x and y directions, for example, $\mu_x^+ a_{i,j} = \frac{1}{2}(a_{i,j} + a_{i+1,j})$. One-sided stencils are used when necessary at the boundary. This discretization is consistent to second-order. Note that the derivatives of the diagonal terms, $\partial \sigma^{xx}/\partial x$ and $\partial \sigma^{yy}/\partial y$, use narrow stencils, benefiting from the staggered grid. In contrast, the derivatives of the

off-diagonal terms, $\partial\sigma^{xy}/\partial x$ and $\partial\sigma^{xy}/\partial y$, must be approximated by wider stencils, the natural choice being central differences.

Having computed the divergence of the conformation tensor at all interior edges, we proceed to compute the velocity field, by solving the linear system of equations:

$$D_x^+ p_{i,j} - (D_x^+ D_x^- + D_x^+ D_x^-)u_{i+1/2,j}$$

$$= \mu \left(\frac{\partial\sigma^{xx}}{\partial x} + \frac{\partial\sigma^{xy}}{\partial y} \right)_{i+1/2,j},$$

$$D_y^+ p_{i,j} - (D_x^+ D_x^- + D_x^+ D_x^-)v_{i,j+1/2}$$

$$= \mu \left(\frac{\partial\sigma^{xy}}{\partial x} + \frac{\partial\sigma^{yy}}{\partial y} \right)_{i,j+1/2},$$

$$D_x^- u_{i+1/2,j} + D_y^- u_{i,j+1/2} = 0, \tag{3.2}$$

where as before, $\mu = (1 - \beta)/(\beta\lambda)$. The boundary conditions are imposed by the use of ghost cells and anti-reflective conditions for the tangential components of the velocity.

With the velocity at hand, we turn to calculate its gradient, which has to be evaluated at cell centers. Once again, diagonal and off-diagonal elements behave differently: the diagonal elements exploit the staggering and result in narrow stencils,

$$\left(\frac{\partial u}{\partial x} \right)_{i,j} = D_x^- u_{i+1/2,j}, \qquad \left(\frac{\partial v}{\partial y} \right)_{i,j} = D_y^- v_{i,j+1/2},$$

which is well-defined at all points. For the off-diagonal elements, we are forced to resort again to wide-stencil central differences:

$$\left(\frac{\partial v}{\partial x} \right)_{i,j} = \mu_y^- D_x^0 v_{i,j+1/2}, \qquad \left(\frac{\partial u}{\partial y} \right)_{i,j} = \mu_x^- D_y^0 u_{i+1/2,j}.$$

Our choice of discrete operators satisfies the relation $\nabla^2 \boldsymbol{u} = \nabla \cdot \nabla \boldsymbol{u}$, so that the discrete velocity satisfies a finite-dimensional constrained optimization equation approximating (2.3).

The evolution of the conformation tensor is then dictated by substituting the above expressions into the constitutive equation:

$$\frac{\mathrm{d}}{\mathrm{d}t}\sigma_{i,j}^{xx} = -D_x^-(u_{i+1/2,j}\,\mu_x^+\sigma_{i,j}^{xx}) - D_y^-(v_{i,j+1/2}\,\mu_y^+\sigma_{i,j}^{xx})$$

$$+ 2\,\sigma_{i,j}^{xx}\left(\frac{\partial u}{\partial x}\right)_{i,j} + 2\,\sigma_{i,j}^{xy}\left(\frac{\partial u}{\partial y}\right)_{i,j} - \frac{1}{\lambda}(\sigma_{i,j}^{xx} - 1),$$

$$\frac{\mathrm{d}}{\mathrm{d}t}\sigma_{i,j}^{xy} = -D_x^-(u_{i+1/2,j}\,\mu_x^+\sigma_{i,j}^{xy}) - D_y^-(v_{i,j+1/2}\,\mu_y^+\sigma_{i,j}^{xy})$$

$$+ \sigma_{i,j}^{xx}\left(\frac{\partial v}{\partial x}\right)_{i,j} + \sigma_{i,j}^{yy}\left(\frac{\partial u}{\partial y}\right)_{i,j} - \frac{1}{\lambda}\sigma_{i,j}^{xy},$$

$$\frac{\mathrm{d}}{\mathrm{d}t}\sigma_{i,j}^{yy} = -D_x^-(u_{i+1/2,j}\,\mu_x^+\sigma_{i,j}^{yy}) - D_y^-(v_{i,j+1/2}\,\mu_y^+\sigma_{i,j}^{yy})$$

$$+ 2\,\sigma_{i,j}^{xy}\left(\frac{\partial v}{\partial x}\right)_{i,j} + 2\,\sigma_{i,j}^{yy}\left(\frac{\partial v}{\partial y}\right)_{i,j} - \frac{1}{\lambda}(\sigma_{i,j}^{yy} - 1). \tag{3.3}$$

The stationary solution of the continuous systems, $\boldsymbol{\sigma}_{i,j} = \boldsymbol{\Sigma}$, $u_{i+1/2,j} = y_j$, $v_{i,j+1/2} = 0$ solves the discrete system (3.3) as well. Linearizing the discrete system, Fourier expanding along the x-coordinate, we obtain, for every wave number k, a $3n$-dimensional linear eigenvalue problem which can be solved by standard methods (the $3n$ independent variables are the perturbed stress components $\delta\boldsymbol{\sigma}_{i,j}$, with i fixed and $j = 1, 2, \ldots, n$).

3.2. Staggered discretization of tensor fields

We next describe a different discretization, which uses a staggered discretization for tensor fields as well, keeping diagonal elements at cell centers and transferring off-diagonal element to cell corners. Such a staggering has been proposed by Gerritsma [14]. The motivation for this arrangement of tensor field is to obtain maximally compact stencils, since wide stencils often cause the appearance of spurious "checkerboard" modes. In the above central difference scheme, the gradient of vector fields and the divergence of tensor fields use (in part) central differences, and the composition of these two operators yields a wide-stencil discrete Laplacian, which does not preserve the negative-definiteness of the Laplacian. This can be remedied by resorting to a staggered discretization.

The discrete geometry of the "staggered scheme" is shown in Fig. 2. The velocity field uses the same Marker-and-Cell discretization, except for a vertical shift of half a cell, so that the boundaries intersect the first and last computational cells. The discrete velocity variables are now denoted by $u_{i+1/2,j}$, with $j = 0, 1, \ldots, n$, and $v_{i,j+1/2}$, with $j = 0, 1, \ldots, n - 1$; the pressure variables, which are cell-centered, are denoted by $p_{i,j}$, $j = 1, 2, \ldots, n - 1$. The main change affects the discretization of the conformation
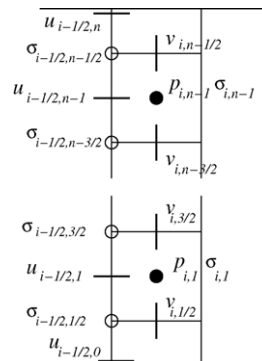

Fig. 2. Discrete geometry for the staggered scheme.

tensor: its diagonal elements remain cell-centered, and are denoted by $\sigma_{i,j}^{xx}, \sigma_{i,j}^{yy}$, $j = 1, 2, \ldots, n - 1$. The off-diagonal elements are now defined at cell corners and are denoted by $\sigma_{i+1/2, j+1/2}^{xy}$, $j = 0, 1, \ldots, n - 1$. In this new setting there are $3n - 2$ degrees of freedom per computational column: the $2(n - 1)$ variables $\sigma_{i,j}^{xx}, \sigma_{i,j}^{yy}$, and the n variables $\sigma_{i+1/2, j+1/2}^{xy}$.

As above, the first step is the calculation of $\nabla \cdot \boldsymbol{\sigma}$, which now benefits from a compact stencil in all its elements:

$$\left(\frac{\partial \sigma^{xx}}{\partial x} + \frac{\partial \sigma^{xy}}{\partial y}\right)_{i+1/2, j} = D_x^+ \sigma_{i,j}^{xx} + D_y^+ \sigma_{i+1/2, j-1/2}^{xy},$$

$$i = 1, 2, \ldots, n - 1,$$

$$\left(\frac{\partial \sigma^{xy}}{\partial x} + \frac{\partial \sigma^{yy}}{\partial y}\right)_{i, j+1/2} = D_x^+ \sigma_{i-1/2, j+1/2}^{xy} + D_y^+ \sigma_{i,j}^{yy},$$

$$j = 1, 2, \ldots, n - 1. \tag{3.4}$$

With $\nabla \cdot \boldsymbol{\sigma}$ at hand, the velocity field is computed by solving the elliptic system (3.2). This time, no ghost cells nor reflections are needed, as $u_{i-1/2, 0} = -1/2$, $u_{i-1/2, n} = 1/2$, and by the incompressibility condition, $v_{i, j+1/2} = 0$ for $j = 0, n - 1$.

We then turn to calculate the velocity gradient, whose diagonal elements are defined at cell centers and its off-diagonal elements at cell corners. Again, we benefit from fully compact stencils:

$$\left(\frac{\partial u}{\partial x}\right)_{i,j} = D_x^- u_{i+1/2, j}, \qquad \left(\frac{\partial u}{\partial y}\right)_{i+1/2, j+1/2} = D_y^+ u_{i+1/2, j},$$

$$\left(\frac{\partial v}{\partial y}\right)_{i,j} = D_y^- v_{i, j+1/2}, \qquad \left(\frac{\partial v}{\partial x}\right)_{i+1/2, j+1/2} = D_x^+ v_{i, j+1/2}.$$

Problems start now that we need to substitute the velocity gradient into the third equation in (2.4). The staggered discretization of tensor fields was designed to optimally fit the differential operators. It is however unclear how to define the product of two tensors when their diagonal and off-diagonal elements are defined at different points (it is also unclear how to define positive-definiteness in this setting). Specifically, the calculation of (2.4) requires σ^{yy} at cell corners, and $\sigma^{xy}, \partial u/\partial y$, and $\partial v/\partial x$ at cell centers. The natural solution is to resort to second-order averaging: whenever a cell-centered variable is needed at a cell's corner it is obtained by averaging over the four nearest cell centers; the same applies when a corner variable is needed at a cell's center. Second-order extrapolations are used at boundary cells. For notational simplicity, we denote the cell-to-corner and corner-to-cell interpolated fields by overlines.

The resulting scheme is

$$\frac{d}{dt}\sigma_{i,j}^{xx} = -D_x^-(u_{i+1/2, j} \mu_x^+ \sigma_{i,j}^{xx}) - D_y^-(v_{i, j+1/2} \mu_y^+ \sigma_{i,j}^{xx})$$

$$+ 2\sigma_{i,j}^{xx}\left(\frac{\partial u}{\partial x}\right)_{i,j} + 2\sigma_{i,j}^{xy}\overline{\left(\frac{\partial u}{\partial y}\right)}_{i,j} - \frac{1}{\lambda}(\sigma_{i,j}^{xx} - 1),$$

$$\frac{d}{dt}\sigma_{i+1/2, j+1/2}^{xy} = -D_x^-(\bar{u}_{i+1, j+1/2}\, \mu_x^+ \sigma_{i+1/2, j+1/2}^{xy})$$

$$- D_y^-(\bar{v}_{i+1/2, j+1}\, \mu_y^+ \sigma_{i+1/2, j+1/2}^{xy})$$

$$+ \bar{\sigma}_{i+1/2, j+1/2}^{xx}\left(\frac{\partial v}{\partial x}\right)_{i+1/2, j+1/2}$$

$$+ \bar{\sigma}_{i+1/2, j+1/2}^{yy}\left(\frac{\partial u}{\partial y}\right)_{i+1/2, j+1/2} - \frac{1}{\lambda}\sigma_{i,j}^{xy},$$

$$\frac{d}{dt}\sigma_{i,j}^{yy} = -D_x^-(u_{i+1/2, j}\, \mu_x^+ \sigma_{i,j}^{yy}) - D_y^-(v_{i, j+1/2}\, \mu_y^+ \sigma_{i,j}^{yy})$$

$$+ 2\sigma_{i,j}^{xy}\overline{\left(\frac{\partial v}{\partial x}\right)}_{i,j} + 2\sigma_{i,j}^{yy}\left(\frac{\partial v}{\partial y}\right)_{i,j} - \frac{1}{\lambda}(\sigma_{i,j}^{yy} - 1). \tag{3.5}$$

As above, the corresponding spectrum can be computed by standard methods.

3.3. Numerical results

In this subsection we present calculations of the stability spectrum using the two numerical schemes. Throughout this paper we use a viscosity ratio of $\beta = 0.2$. The number of grid points along the vertical mesh is $n = 196$ unless otherwise specified.

3.3.1. Central difference scheme

A typical spectrum is shown in Fig. 3 for $\lambda = 1$, $k = 1$. The eigenvalues are measured in units of $1/\lambda$; in these units the continuous GL strip has real part -1, whereas the continuous viscous strip has real part $-1/\beta = -5$. The computed spectrum is very different than the analytical one: the GL strip has an oval shape, similar to that reported in the literature. The second strip is also split, and connects to the GL strip by a horizontal strip of eigenvalues. At higher values of λ (and k), the splitting of the GL strip is even more pronounced,
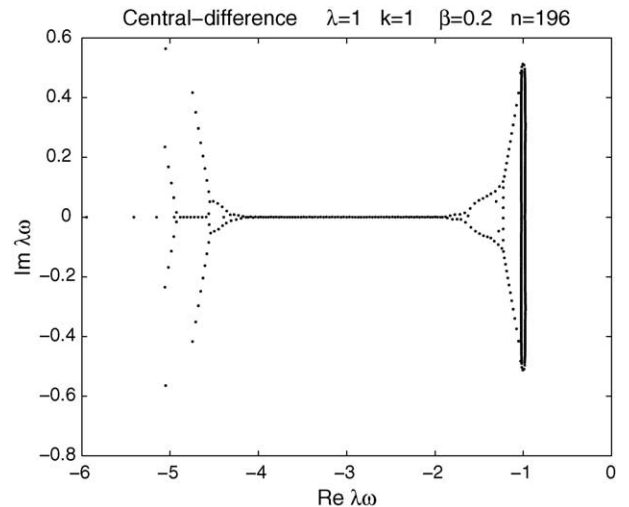

Fig. 3. Central-difference scheme: stability spectrum for $\lambda = 1$ and $k = 1$.

and eventually, some of the computed eigenvalues protrude into the right half plane, implying that the computed Couette flow is linearly unstable. For $n = 196$ points, the loss of stability occurs already at $\lambda \approx 10$. In agreement with previous work, the convergence of the spectrum to the analytical one, as $n \to \infty$, is very slow.

3.3.2. Staggered scheme

In Figs. 4 and 5 we present stability spectra obtained with the staggered scheme; the difference with the finite-difference scheme is striking. Fig. 4 shows the spectrum for $\lambda = 1$ and $k = 1$. The computed spectrum agrees perfectly with the analytical prediction. There are two vertical strips of singular eigenvalues with real parts $\mathfrak{Re}\,\lambda\omega = -1$ and $\mathfrak{Re}\,\lambda\omega = -5$, respectively, two discrete GL eigenvalues, which coincide with the predicted values within six significant digits, and a small number of discrete viscous eigenvalues. To the best of our knowledge, this is the first reported calculation that produces a spectrum in which the continuous strips of eigenvalues remain straight lines within 7–8 significant digits.
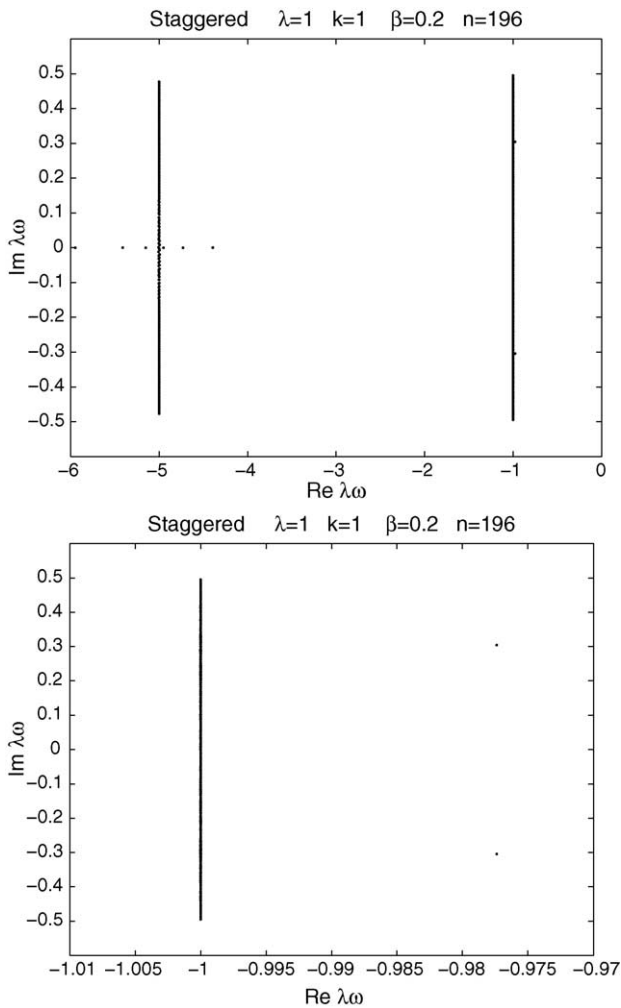
Fig. 4. Staggered scheme: stability spectrum for $\lambda = 1$ and $k = 1$. The figure on the bottom shows a magnification of the GL spectrum.
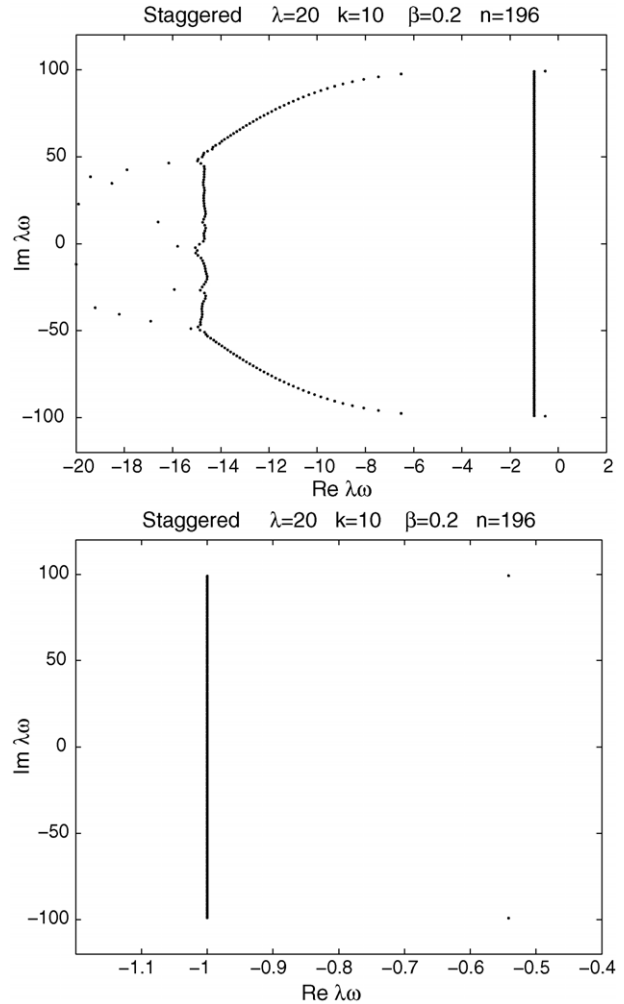
Fig. 5. Staggered scheme: stability spectrum for $\lambda = 20$ and $k = 10$. The figure on the bottom shows a magnification of the GL spectrum.
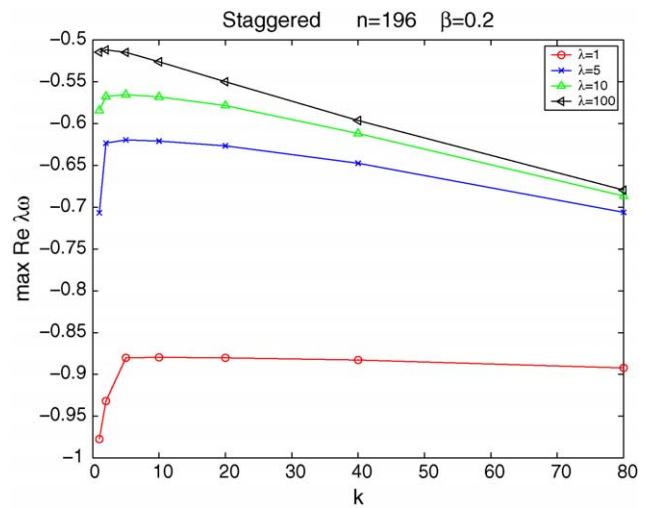

Fig. 6. Staggered scheme: the real part of the least stable eigenvalue as function of the wavenumber k for several values of the Weissenberg number.

The stability spectrum for $\lambda = 20$ and $k = 10$ is shown in Fig. 5. The GL part of the spectrum retains its perfect structure, with the continuous part lying on the line $\Re e\, \lambda\omega = -1$ within 7–8 significant digits. The viscous part of the spectrum, however, distorts, becoming however even more stable.

In Fig. 6 we plot the real part of the least stable eigenvalue (the discrete GL mode) for different value of λ. In agreement with the analytical prediction, $\Re e\, \lambda\omega$ is an increasing function of λ but remains strictly below $-1/2$. Thus, the staggered scheme seems immune to spurious linear instabilities at all ranges of parameters.

Much insight is gained by examining the computed eigenfunctions. In Fig. 7 we plot eigenfunctions corresponding to discrete GL and viscous eigenvalues. The eigenfunctions are
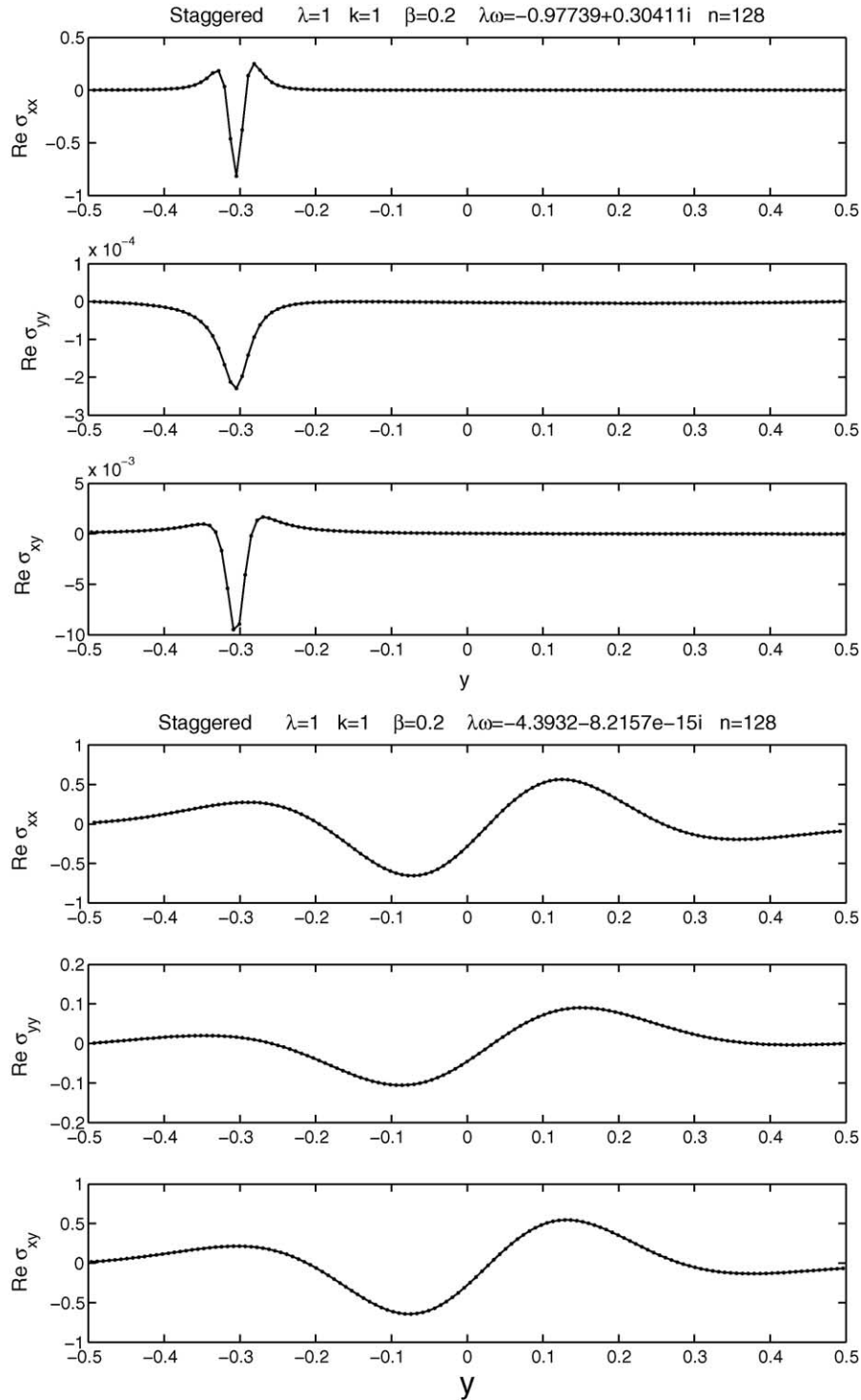
Fig. 7. Staggered scheme: eigenfunctions corresponding to a discrete GL eigenvalue (top) and a discrete viscous eigenvalue (bottom).

extended and smooth, which explains why they can be well approximated at relatively coarse resolution.

More interesting is the structure of the eigenvectors corresponding to the singular eigenvalues, shown in Fig. 8. The top portion of this figure shows the three components of the eigenvector $\delta\sigma$ for a singular GL mode. The function $\delta\sigma^{yy}$ differs from zero (within negligible errors) at a single

point, i.e., is a discrete approximation to a delta-function. Likewise, the functions $\delta\sigma^{xy}$ and $\delta\sigma^{xx}$ differ from zero at two and three points, respectively, and thus approximate first and second derivatives of a delta function. The staggered discretization correctly captures the structure of the continuous GL modes, which explains why the eigenvalues can be predicted with such high accuracy. Note that as
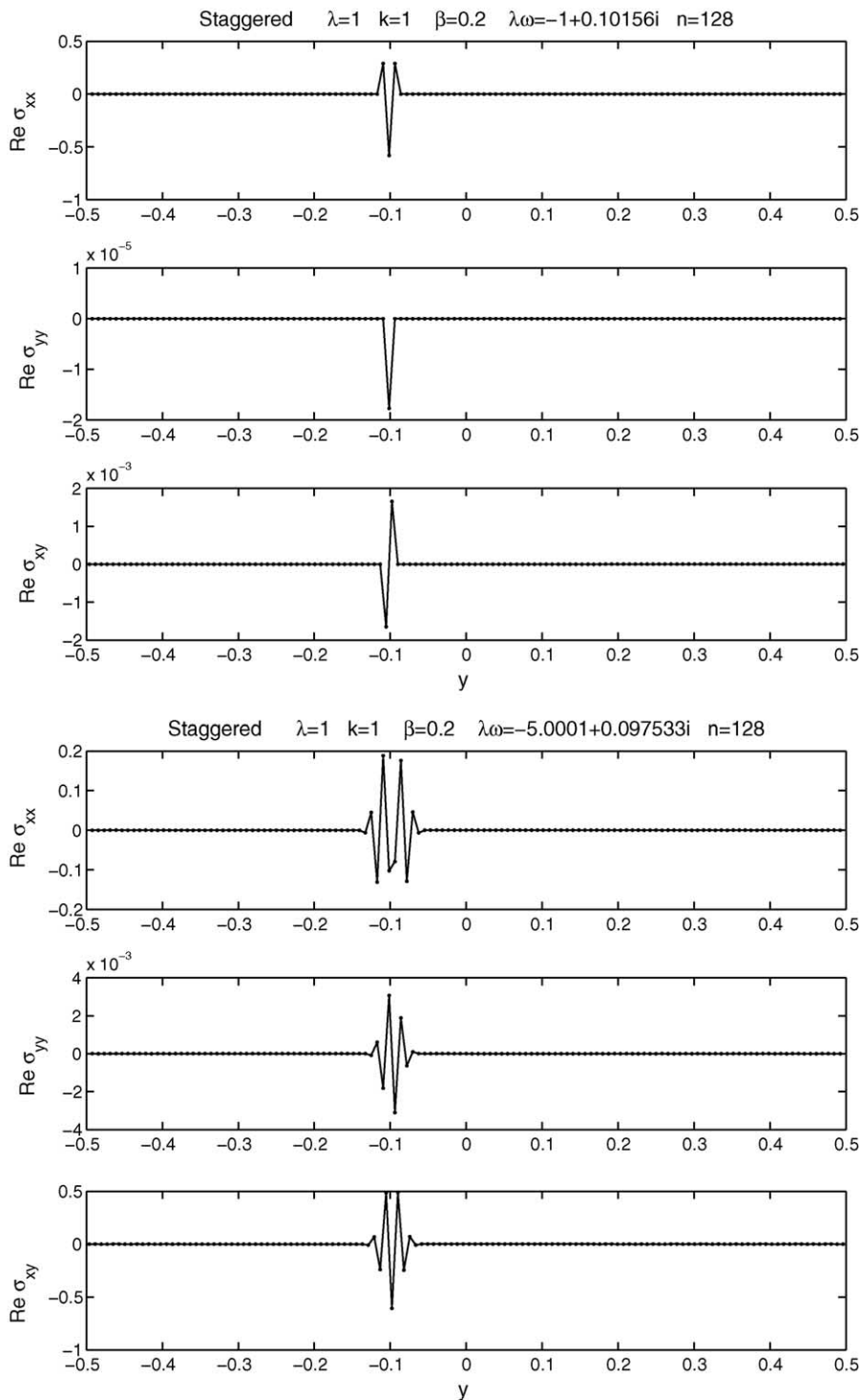
Fig. 8. Staggered scheme: eigenfunctions corresponding to a singular GL eigenvalue (top) and a singular viscous eigenvalue (bottom).

$n \to \infty$, the computed eigenvectors do not converge to a smooth function. The support of these eigenvectors shrinks as n grows, so that convergence takes place in the space of distributions.

The lower portion of Fig. 8 shows the three components of the eigenvector $\delta\sigma$ for a singular viscous mode. The discrete eigenfunctions are dominated by the distributional nature of the eigenfunctions, i.e., they behave like high-order derivatives of the delta distribution, as predicted in Section 2.3.

One may wonder why calculations that are based on "velocity formulations" show a splitting of the continuous spectra, although the singular pure-stress eigenmodes are being filtered out. While the Graham-type eigenfunctions are continuously differentiable, their third and fourth derivatives, which are present in the equations, exhibit delta-singularities, and therefore challenge computational schemes in a way that is similar to the pure stress modes.

3.4. Stability spectrum for Poiseuille flow

One may wonder at this point whether the use of staggered tensor fields is essential for an accurate approximation of the conformation tensor. The question is whether the accurate reproduction of the stability spectrum for Couette flow is "accidental", or, whether it is due to some exceptional property of the staggered scheme. As a simple test, we briefly consider the closely related problem of Poiseuille flow for an Oldroyd-B fluid. There, the steady velocity profile is given by

$$U(y) = 4(y - \tfrac{1}{2})^2,$$

and the singular spectrum analogous to the singular GL spectrum lies on the segment $\omega + \lambda^{-1} + ikU(y) = 0$. The main difference between Couette and Poiseuille flow is that the GL-like singular eigenfunctions for Poiseuille flow are not
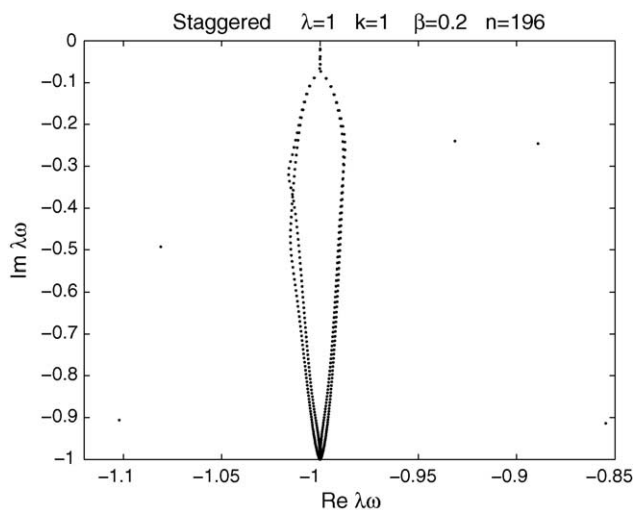
supported at a single point, i.e., the structure of the singularity is different.

The computed spectrum for $\lambda = 1$ and $k = 1$ is depicted in Fig. 9. The computation uses the staggered scheme, yet the accuracy of the spectrum is comparable to that obtained with a non-staggered scheme, and the usual splitting of the singular spectrum occurs. An eigenfunction associated with one of the singular eigenvalues is shown in Fig. 10; it is less localized than for Couette flow, and the singularity seems to be dominated by a regularized power-law divergence. Moreover, there is no decoupling between the conformation tensor and the velocity field. Thus, we conclude that the success of the staggered scheme for Couette flow is in some sense "accidental", and due to the very special nature of the eigenfunctions.

4. Non-normality, pseudo-spectra and transients

Spectral calculations have been a standard tool in the study of differential equations for a long time. As commented in a review by Trefethen [23], spectral computations are useful for three basic reasons: (i) a physical reason – the eigenvalues provide information about the behavior of the system, (ii) an algorithmic reason – transformation into a basis of eigenfunctions may speed up computations, and (iii) a psychological reason – the spectrum provides a simplified picture of the system as a set of points in the complex plane.

There is a growing awareness, however, that spectral analysis may in certain cases lead to erroneous conclusions. This may happen in problems in which the linear operator is non-normal. A normal operator is one that has a complete set of orthogonal eigenfunctions, or equivalently, commutes with its adjoint. In contrast, the eigenfunctions of a non-normal operator are not orthogonal and may not span the entire linear space. Even if the eigenfunctions do form a complete set, the change into eigenfunction coordinates may involve extreme distortions of the space, which from a computational point of view are ill-conditioned. Generally, the spectral properties of non-normal operators do not necessarily determine the stability of the system: the spectrum of a non-normal operator can even be empty, and examples can be constructed where the spectrum lies entirely on the left half plane, but yet, the system is linearly unstable (e.g, the Zabczyk example in [23]).

The study of non-normal matrices and operators goes back to the beginning of the 20th century. There has been a renewed activity in this field in the last 15 years, where the stability analysis of many physical systems has been re-examined with new computational tools dedicated to the study of non-normal operators. A classical example where a discrepancy exists between predictions based on spectral analysis and experiments is Poiseuille (Newtonian) flow in a pipe: spectral analysis predicts stable behavior for arbitrarily large Reynolds number, whereas transition to turbulence typically occurs in the laboratory at a Reynolds number in the vicinity of 2000. This discrepancy has been analyzed in [24] with emphasis on the

Fig. 9. Poiseuille flow with the staggered scheme: the right-most part of the spectrum for $\lambda = 1$ and $k = 1$.

role played by non-normality on the amplification of small perturbations toward a nonlinear regime (see Orszag and Patera [25] for a thorough investigation of the mechanism that leads to turbulence). The role of non-normality in a viscoelastic context was shortly discussed by Atalik and Keunings [26]

who considered the transition from linear to nonlinear evolution of perturbations.

One of the main tools in the study of non-normal operators is the resolvent. The resolvent of an operator A is a mapping $z \mapsto (zI - A)^{-1}$ with $z \in \mathbb{C}$. It is defined for z in the resolvent
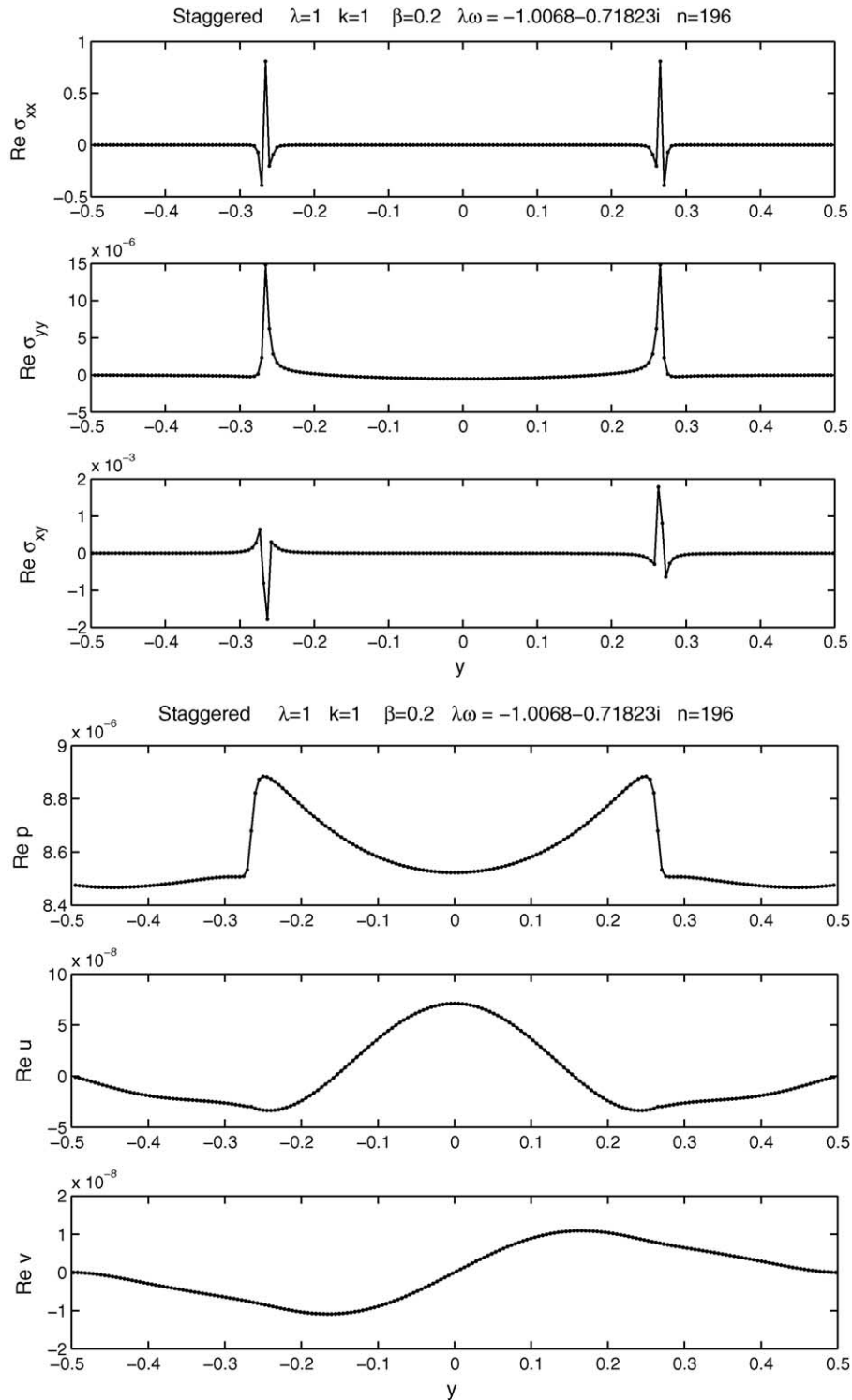
Fig. 10. Poiseuille flow with the staggered scheme: real part of an eigenfunction from the continuous GL strip. The six curves show, from top to bottom, the real part of σ^{xx}, σ^{yy}, σ^{xy}, p, u, and v. The parameters are $\lambda = 1$ and $k = 1$.

set, which is the complement of its spectrum $\Lambda(A)$. The ϵ-pseudo-spectrum of the operator A is defined as

$$\Lambda_\epsilon(A) = \left\{ z : \|(A - zI)^{-1}\| \geq \frac{1}{\epsilon} \right\},$$

i.e., it is a subset of the resolvent set for which the resolvent operator has sufficiently large norm. Here and below, norms correspond to the Euclidean vector norm and its subordinate matrix norm. Equivalently, it can be defined as the closure of the set

$$\Lambda_\epsilon(A) = \{z : \exists B, \|B\| \leq \epsilon, z \in \Lambda(A + B)\}.$$

The latter definition has a more intuitive interpretation. The number $z \in \mathbb{C}$ belongs to the ϵ-pseudo-spectrum of A if it

belongs to the spectrum of a perturbation of A, where the norm of the perturbation is smaller than ϵ. Since computations always involve perturbations of operators (due to truncation and roundoff errors), the pseudo-spectrum represents a range of behaviors that one could expect in an actual computation.

In Fig. 11 we plot pseudo-spectral contour lines for $k = 1$ and $\lambda = \{1, 10, 100\}$. The contours are labeled in logarithmic units. These computations were performed with the Eigtool Matlab Toolbox [27]. Roughly speaking, the contour lines to the right of the singular GL spectrum are vertical. For $\lambda = 1$, even perturbations with norm as large as $\epsilon = 10^{-1}$ do not suffice to turn the system linearly unstable. For $\lambda = 10$ perturbation with norm as small as 10^{-5} can lead to instability, whereas for $\lambda = 100$ unstable behavior may occur due to perturbations with norm $10^{-7.5}$. This gives another perspective on why instabilities occur at large enough
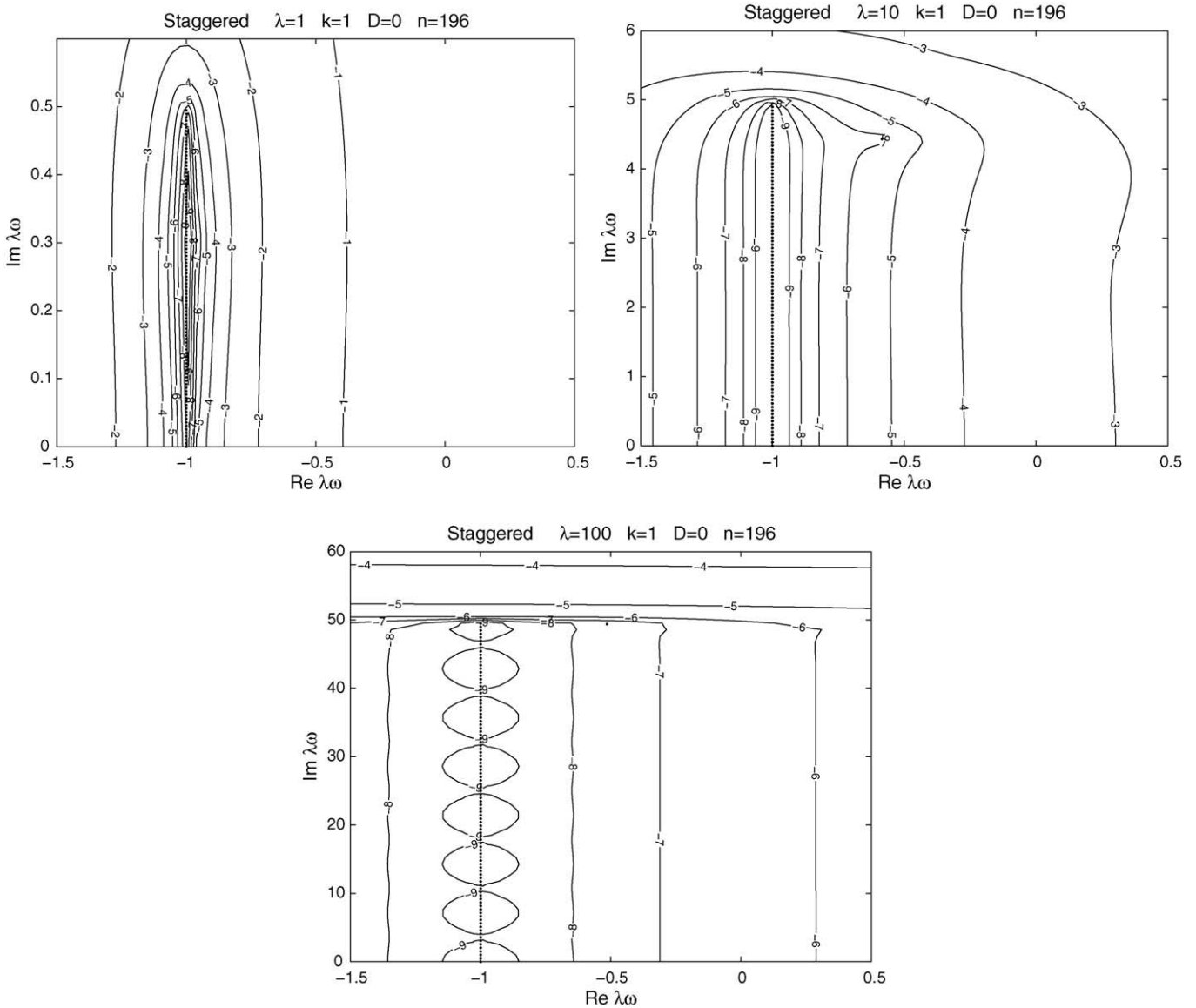

Fig. 11. Contour lines of the pseudo-spectra for $k = 1$ and (a) $\lambda = 1$, (b) $\lambda = 10$, and (c) $\lambda = 100$, The contours are labeled using a $\log_{10}$ scale. The computation uses the staggered discretization with $n = 196$ points, and the Eigtool Matlab Toolbox for the evaluation of the pseudo-spectra.

Weissenberg number, without yet revealing the destabilizing mechanism.

Pseudo-spectral calculations provide also information about the magnitude of transient growth. If for some $\epsilon > 0$ and constant C:

$$\alpha_\epsilon(A) \equiv \max_{\lambda \in \Lambda_\epsilon(A)} \Re e \, \lambda > C,$$

then

$$\sup_{t>0} \|e^{tA}\| > \frac{C}{\epsilon}.$$

The real number $\alpha_\epsilon(A)$ is called the ϵ-pseudo-spectral abscissa, and corresponds to the real part of the least-stable element of the pseudo-spectrum. Thus, if the ϵ-pseudo-spectra protrude significantly into the positive reals for small ϵ, then

the norm of the evolution operator exceeds at some intermediate time a bound inversely proportional to ϵ. The proof is in fact very simple [28]. Let $z \in \Lambda_\epsilon(A)$ have positive real part. Then, from the Laplace transform identity:

$$(zI - A)^{-1} = \int_0^\infty e^{-tz} e^{tA} \, dt,$$

it follows that

$$\frac{1}{\Re e \, z} \sup_{t>0} \|e^{-tA}\| \geq \int_0^\infty e^{-t \Re e \, z} \|e^{tA}\| \, dt \geq \left\| \int_0^\infty e^{-tz} e^{tA} \, dt \right\|$$

$$= \|(zI - A)^{-1}\| \geq \frac{1}{\epsilon},$$

where the last inequality follows from the definition of the ϵ-pseudo-spectrum. Since this inequality holds for any $z \in$
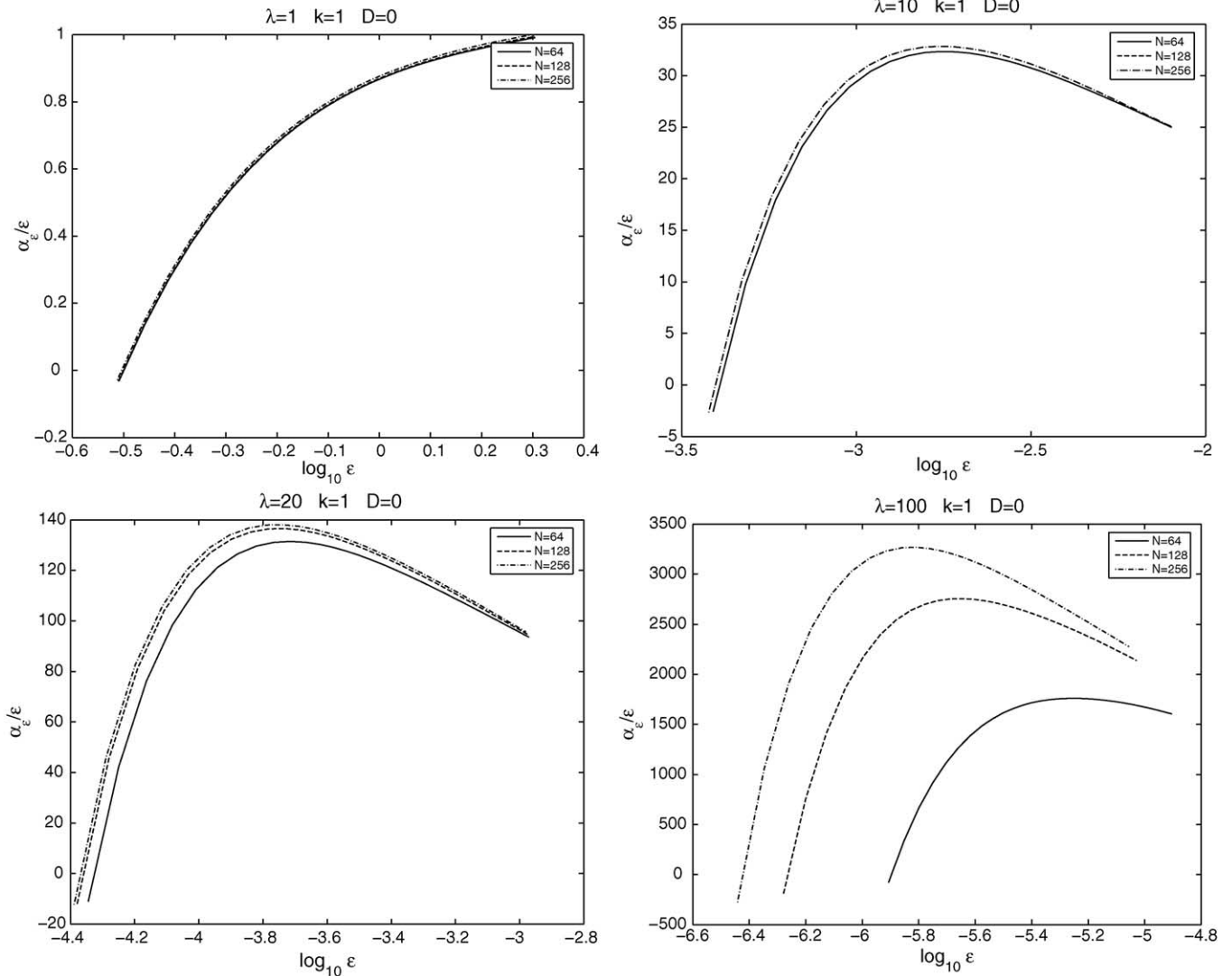

Fig. 12. The scaled ϵ-pseudo-spectral abscissa $\alpha_\epsilon(A)/\epsilon$ vs. $\log_{10} \epsilon$ for $k = 1$ and (a) $\lambda = 1$, (b) $\lambda = 10$, (c) $\lambda = 20$, and (d) $\lambda = 100$. The three lines in each graph correspond to computations with $n = 64$ points (solid lines), $n = 128$ points (dashed lines), and $n = 256$ points (dash-dotted lines).

$\Lambda_\epsilon(A)$ and $\epsilon > 0$, it follows that

$$\sup_{t>0} \|e^{-tA}\| \geq \sup_{\epsilon>0} \frac{\alpha_\epsilon(A)}{\epsilon}. \tag{4.1}$$

Inequality (4.1) states that the maximum value of $\alpha_\epsilon(A)/\epsilon$, taken over all values of ϵ, is a lower bound on the maximum transient amplification. That is, there exists a time t_0 and a vector u (the initial conditions), such that

$$\|e^{-t_0 A} u\| \geq \sup_{\epsilon>0} \frac{\alpha_\epsilon(A)}{\epsilon} \|u\|.$$

In Fig. 12 we plot the value of $\alpha_\epsilon(A)/\epsilon$ versus $\log_{10} \epsilon$ for $k = 1$ and various values of λ. Each graph shows three curves corresponding to different level of refinement. The graphs for $\lambda \leq 20$ seem to have converged, whereas the computation for $\lambda = 100$ has not yet reached a converging regime, even for $n = 256$ points.

From Fig. 12c, for example, we deduce the existence of an initial perturbation, which, for $\lambda = 20$, is amplified, at some intermediate time by a factor of a least 140. For $\lambda = 100$, the transient amplification may exceed a factor of several thousands.

A direct verification of the extent of transient amplification can be computed by exponentiating numerically the difference operator and calculating the norm of the resulting evolution operator. The results are shown in Fig. 13. Again, three levels of refinement are used to assess the accuracy of the results. Here too, the results seem to converge well for $\lambda \leq 20$. As expected, the maximal transient amplification exceeds the lower bound deduced from Fig. 12. The duration of the transient period of growth is also monotonically increasing with the Weissenberg number.

The initial condition that leads to maximum transient amplification can be approximated directly from the (discrete) operator e^{At} via an SVD, with t chosen such to maximize
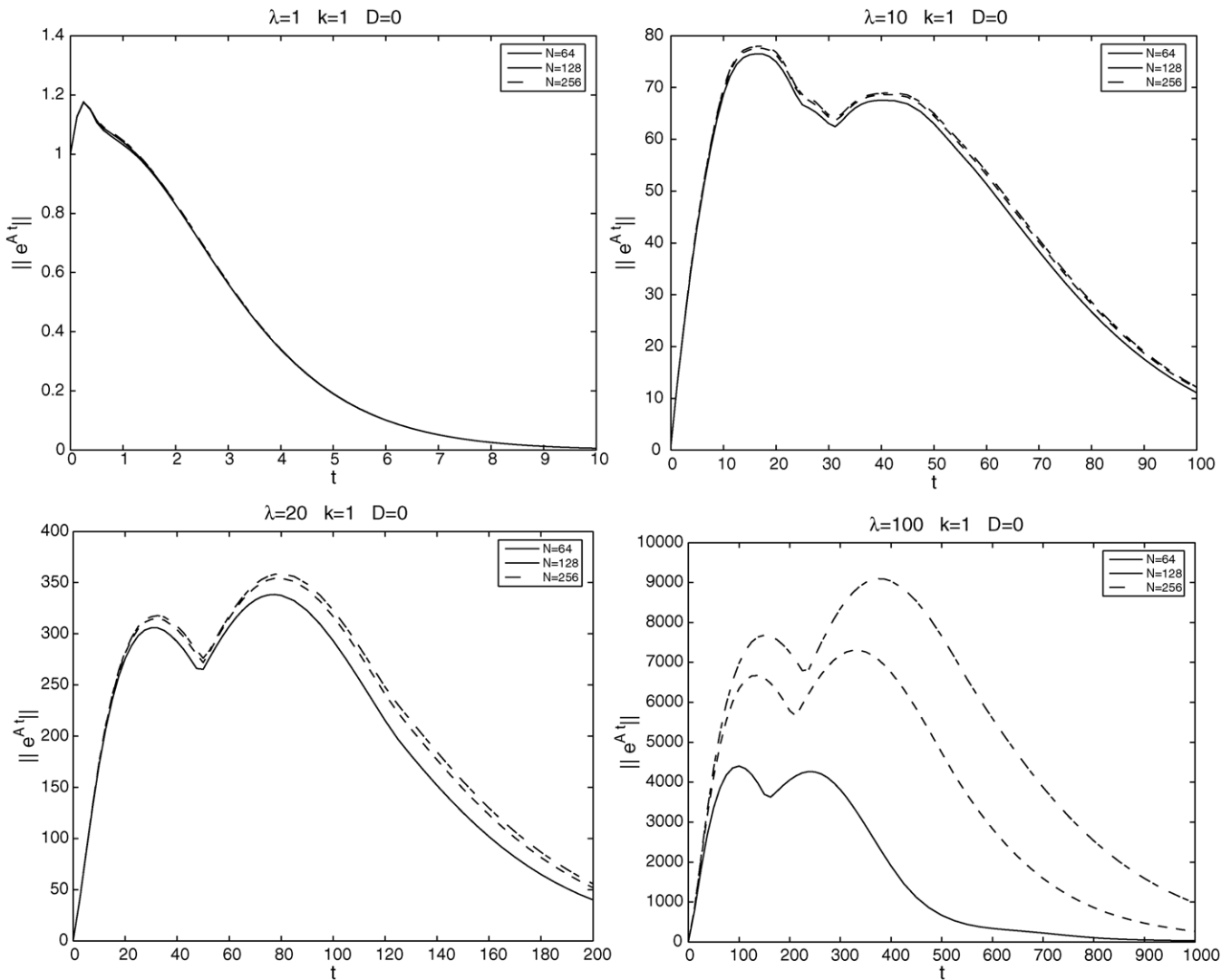

Fig. 13. The norm of the evolution operator e^{At} as function of time for $k = 1$ and (a) $\lambda = 1$, (b) $\lambda = 10$, (c) $\lambda = 20$, and (d) $\lambda = 100$. The three lines in each graph correspond to computations with $n = 64$ points (solid lines), $n = 128$ points (dashed lines), and $n = 256$ points (dash-dotted lines).
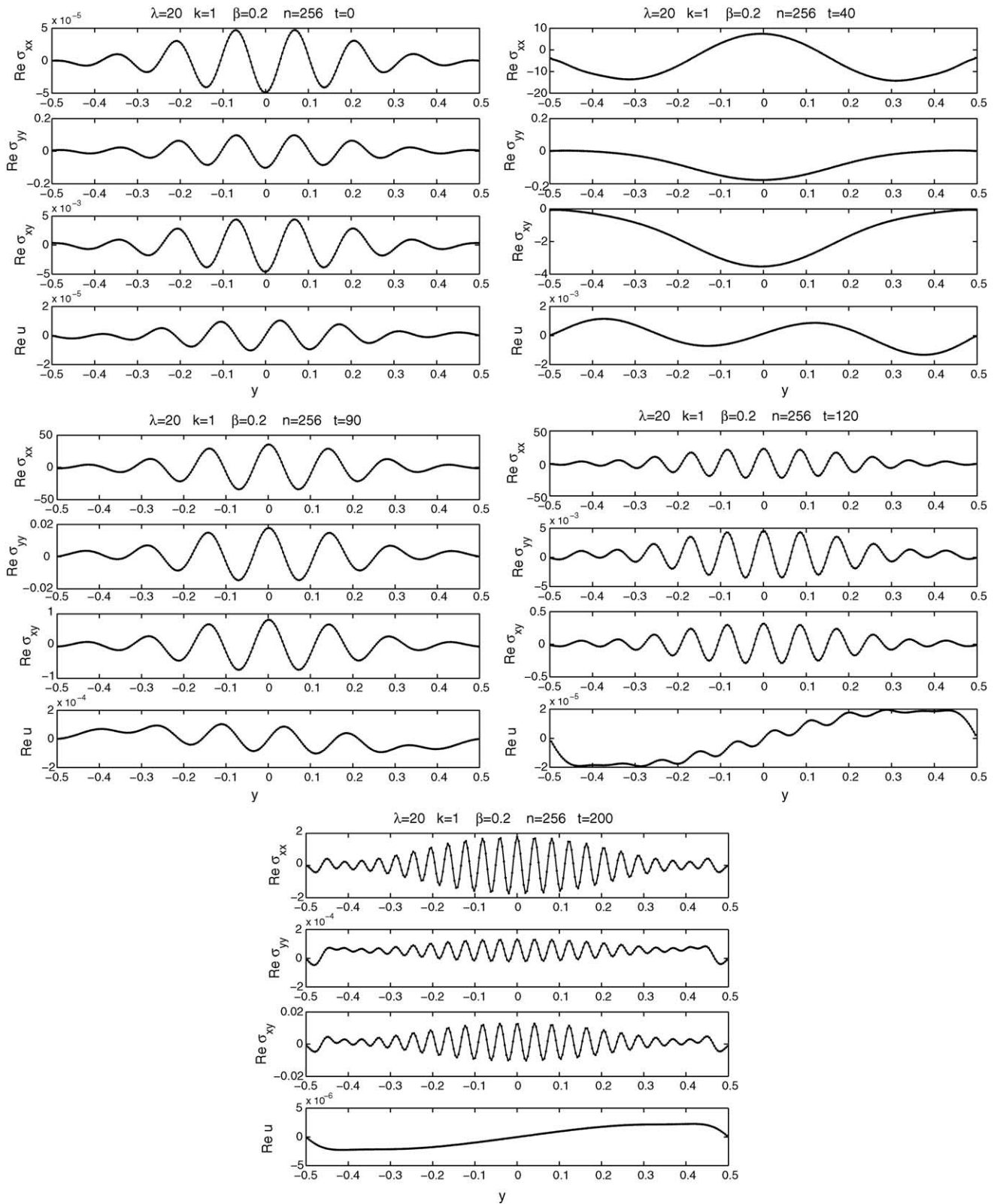
Fig. 14. Time evolution of the most amplified initial perturbation for $k = 1$ and $\lambda = 20$. Each graph shows the real part of the fields σ^{xx}, σ^{yy}, σ^{xy}, and u. The fives graphs correspond to snapshots at time $t = 0, 40, 90, 120, 200$.

the curves in Fig. 13. Thus, we identified the most amplified perturbation for $k = 1$ and $\lambda = 20$; snapshots of its time evolution are depicted in Fig. 14. Although the maximum amplification occurs at time $t = 90$, we observe that while the perturbation decays, it generates spatial oscillations of increasing frequency. At time $t = 200$, the perturbation is still larger in norm than the initial perturbation, while oscillations have a wavelength of several mesh spacings. For slightly longer times this computation, which uses $n = 256$ points, can no longer resolve these cross-stream oscillations.

Note that the velocity component u is significantly smaller in absolute value than the stress components. In fact, the solution shown in Fig. 14 exhibits a stress field with small divergence, which suggests that it might be related to the family of divergence-free stress fields identified in Section 2.2. Set for example an Airy stress function $\phi(x, y) = \sin(\pi x) \cos(\pi y)$ in (2.7). This corresponds to an initial perturbation

$$\delta\boldsymbol{\sigma}(x, y, 0) = \pi^2 \begin{pmatrix} \sin(\pi x)\cos(\pi y) & -\cos(\pi x)\sin(\pi y) \\ -\cos(\pi x)\sin(\pi y) & \sin(\pi x)\cos(\pi y) \end{pmatrix},$$

which for long time $t > \lambda$ is dominated by

$$\delta\boldsymbol{\sigma}(x, y, t) \sim \pi^2 t^2 \mathrm{e}^{-t/\lambda} \ \sin[\pi(x - yt)]\cos(\pi y) \begin{pmatrix} 1 & 0 \\ 0 & 0 \end{pmatrix}.$$
(4.2)

Note how, for fixed x, the spatial frequency increases linearly in time, while the duration of the transient growth scales with the Weissenberg number. Thus, we conclude that the most amplified perturbation is associated with non-modal solutions of the form (2.7).

The interplay between transient amplification and the formation of large cross-stream gradients can also be seen through the integral formulation of the constitutive equation:

$$\boldsymbol{\sigma}(\boldsymbol{x}, t) = \mathrm{e}^{-t/\lambda} \boldsymbol{F}(\boldsymbol{x}, t, 0)\boldsymbol{\sigma}(\boldsymbol{x}, 0)\boldsymbol{F}^{\mathrm{T}}(\boldsymbol{x}, t, 0)$$
$$+ \frac{1}{\lambda} \int_0^t \mathrm{e}^{-(t-s)/\lambda} \boldsymbol{F}(\boldsymbol{x}, t, s)\boldsymbol{F}^{\mathrm{T}}(\boldsymbol{x}, t, s) \, \mathrm{d}s,$$

where $\boldsymbol{F}(\boldsymbol{x}, t, s)$ is the relative deformation gradient between time s and t at the Lagrangian coordinate $\boldsymbol{x}$. The steady solution $\boldsymbol{\sigma}(\boldsymbol{x}, t) = \boldsymbol{\Sigma}$ is a solution of this integral equation, with

$$\boldsymbol{F}(\boldsymbol{x}, t, s) = \begin{pmatrix} 1 & t \\ 0 & 1 \end{pmatrix}.$$

For $\boldsymbol{\sigma}(\boldsymbol{x}, t) = \boldsymbol{\Sigma} + \delta\boldsymbol{\sigma}(\boldsymbol{x}, t)$ with $\delta\boldsymbol{\sigma}(\boldsymbol{x}, 0)$ divergence-free, $\boldsymbol{F}$ remains unchanged, and $\delta\boldsymbol{\sigma}(\boldsymbol{x}, t)$ is explicitly given by

$$\delta\boldsymbol{\sigma}(\boldsymbol{x}, t) = \mathrm{e}^{-t/\lambda} \begin{pmatrix} 1 & t \\ 0 & 1 \end{pmatrix} \delta\boldsymbol{\sigma}(\boldsymbol{x}, 0) \begin{pmatrix} 1 & 0 \\ t & 1 \end{pmatrix}.$$

This expression clarifies how divergence-free stress fields evolve. The deformation gradient, $\boldsymbol{F}$, is responsible for the deformation of the stress perturbation and for the transient growth. The advection by a shearing field is responsible, on the other hand, for the generation of high-frequency cross stream waves.

Thus, as time evolves, "energy" is transfered to high-frequency modes, resulting in cross-stream under-resolution and large truncation errors. Once this happens, the behavior of the system is difficult to predict, and notably, small perturbations may be amplified. Of course, as long as the linearized system is considered, the linear instability is imprinted in the spectrum. The added contribution of the above analysis is the revelation of a mechanism that may cause truncation errors to dominate the numerical solution.

5. Addition of stress diffusivity

The fact that the Oldroyd-B and UCM equations can sustain solutions that are singular is bothersome. By itself, it does not invalidate the model, as long as we have not shown that unphysical singular solutions may evolve from physically significant initial data. Yet, one wonders if the highly non-normal nature of the problem, which makes it so sensitive to perturbations is not an indication of model deficiency. Thoughts along those lines were expressed by El-Kareh and Leal [15], which analyzed the existence of solutions for constitutive models of finitely extensible polymers. Their observation was that all standard methods of proof fail because it is not possible to guarantee the regularity of the stress across streamlines, as there is no interaction between disjoint streamlines. Quoting [15]: "While no proof is provided here that solutions in some Sobolev space fail to exist without the modifications to the model suggested here, it is certainly true that none of the currently available methods to prove existence can be applied successfully. Our point of view is that this is an indication of problems with the model rather than any inadequacy of available mathematical theory."

El-Kareh and Leal showed that existence could be proved (up to a certain a priori assumption) if stress diffusion was added to the constitutive model. That is, a term $D\nabla^2\boldsymbol{\sigma}$ is added to the right hand side of the constitutive law. The addition of stress diffusion has a physical justification, resulting from the Brownian motion of the center of mass of the molecules. In bead-and-springs models from which macroscopic dynamics may be derived (up to the need for closure assumptions in nonlinear models), there is a stochastic force which prevents the springs to collapse to zero length. The same source of randomness should also cause center of mass diffusion, but this component is usually omitted by a "local homogeneity assumption". An estimate for the magnitude of the diffusivity coefficient is given in [15], $D \sim 10^{-9}$. The question is whether such a small parameter has any noticeable effect on the behavior of the system over larger scales.

The addition of stress diffusivity in computations has been considered already by Keiller [9], but only along the

stream-wise direction. The addition of isotropic diffusivity has been studied by Sureshkumar and Beris [16], which reported that the addition of small amount of (artificial) diffusivity has little effect on the regular, spatially extended eigenmodes, while completely changing the nature of the singular spectra; in fact, the singular spectra are destroyed and discrete spectra emerge instead. Stress diffusion is commonly used in turbulent viscoelastic simulations, without which gradients grow unbounded due to the fast mixing of stream lines. In [17], for example, it is argued that stress diffusion is necessary in order to correctly predict the tail of the energy spectrum in turbulent flows.

Fig. 15 shows the stability spectrum for $k = 1$, $\lambda = 1$, and a stress diffusivity coefficient $D = 10^{-4}$. The graphs on the top correspond to the staggered scheme with $n = 128$ and $n = 256$ points, whereas the graphs on the bottom correspond to similar calculations using the central-difference scheme. The first observation, is that in agreement with [16]

the singular spectrum has disappeared, and instead there is a nearly vertical finite array of discrete eigenvalues. Moreover, the right-most part of the graph is nearly identical in all four figures, implying that the sensitivity to the method of computation and to the resolution has been significantly reduced with the addition of stress diffusivity. This is not surprising, as solutions are now much smoother, and therefore truncation errors remain relatively small.

Fig. 16 shows the spectra obtained with the staggered scheme for $k = 1$, $\lambda = 1$ and a diffusivity coefficient of $D = 10^{-6}$ with $n = 64$, $n = 128$, and $n = 256$ points. For $n = 64$ the results seem identical to the diffusionless spectrum, which means that the diffusion length is not resolved. As the number of points increases the structure changes, but even for $n = 256$ it has not yet converged to the true spectrum. Yes, there is a noticeable tendency of stabilization as the spatial resolution approaches the characteristic stress diffusion length.
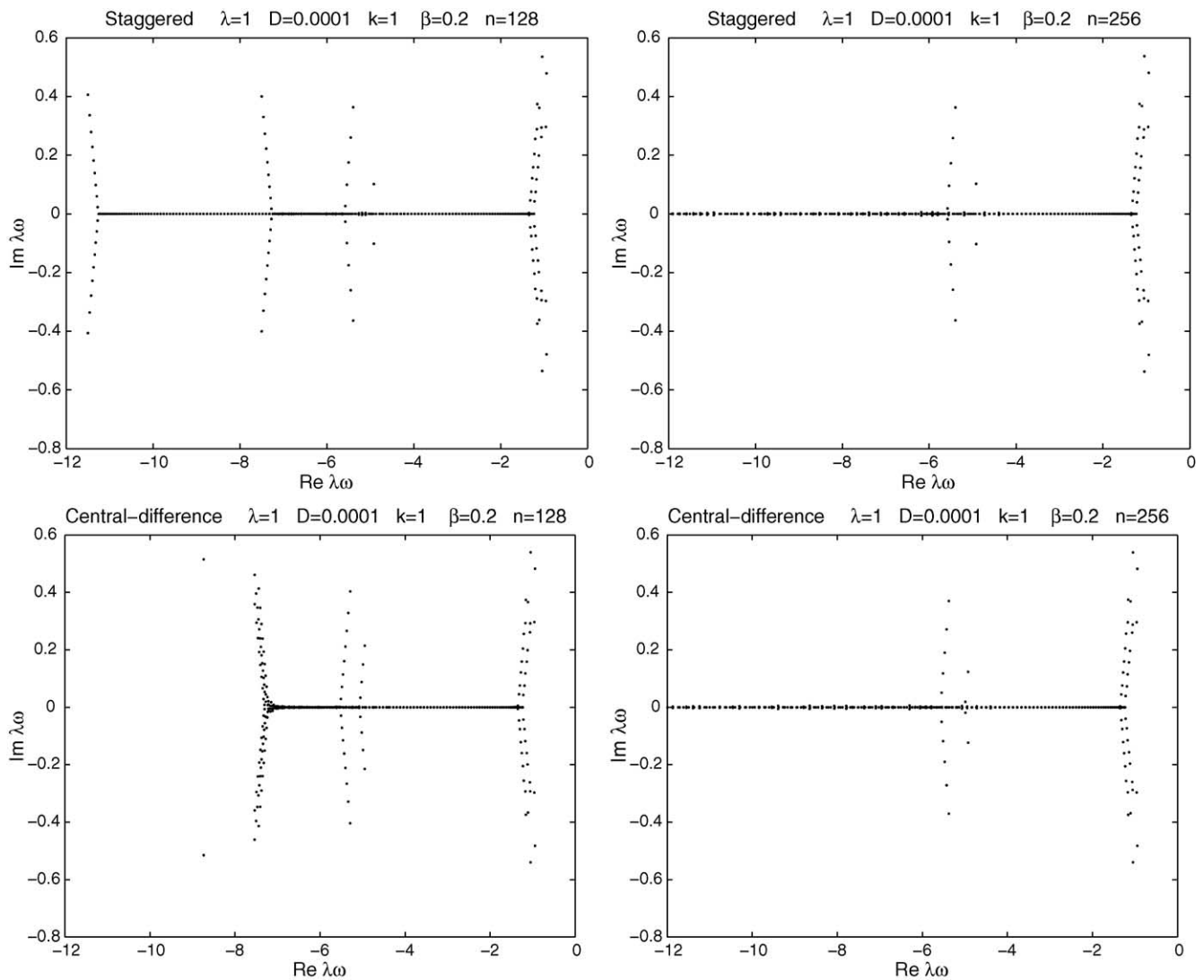

Fig. 15. Stability spectrum for $k = 1$, $\lambda = 1$, and a stress diffusivity constant of $D = 10^{-4}$. The upper row shows results obtained with the staggered scheme with $n = 128$ (left) and $n = 256$ (right) point. The lower row shows the corresponding results obtained with the central-difference scheme.
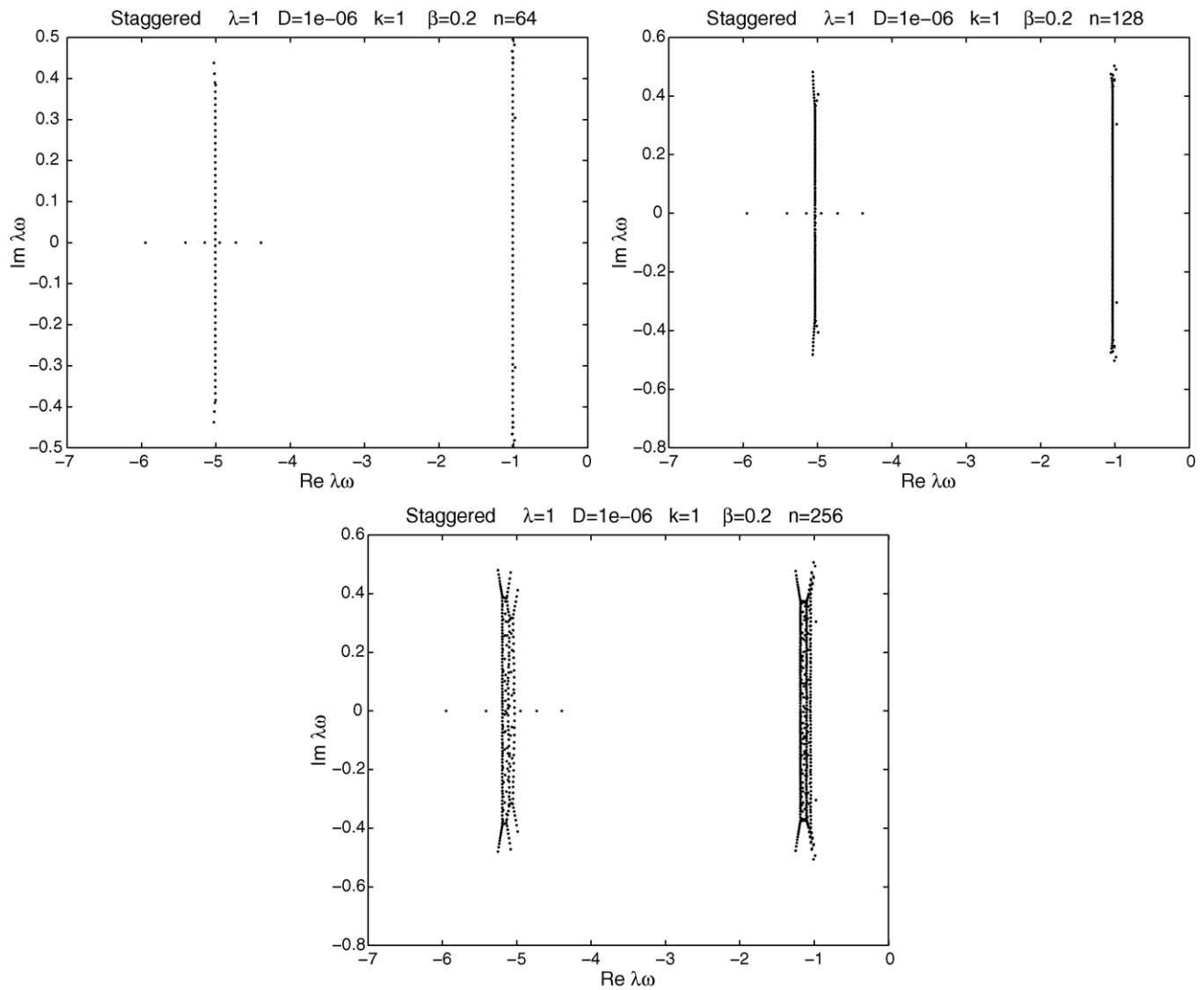
Fig. 16. Stability spectra for $k = 1$, $\lambda = 1$, and a stress diffusivity constant of $D = 10^{-6}$. The results were obtained with the staggered scheme with $n = 64$, $n = 128$, and $n = 256$ points.

6. Conclusions

The main result in this paper is the identification of a family of non-modal stress perturbations of Couette flow, which are divergence free, and therefore do not couple back into the velocity field. These perturbations are exact solutions of the nonlinear system. In particular, there exist initial perturbations in this class, which for high Weissenberg number, exhibit large transient growth accompanied with the formation of cross-stream oscillations whose frequency grows linearly in time. While these perturbations have an asymptotic temporal profile that scales like $t^2 e^{-t/\lambda}$, and therefore eventually decay, the oscillations may, at large enough Weissenberg number, reach sub-grid scales before decaying. We believe this under-resolution effect to be at the heart of the spurious instabilities observed generically in numerical calculations. We emphasize that those oscillatory solutions are not numerical artifacts—they are bona fide solutions of the Oldroyd-B model. Numerical problems arise due to under-resolution.

The fact that the Oldroyd-B model is capable to sustain stress perturbations with arbitrarily large spatial gradients, which do not excite the velocity field is bothersome. This can happen because the stress field interacts with itself only through the induced velocity field, and the latter is unaffected by divergence-free stress components. It has been argued in the past that stress diffusion becomes important at sufficiently small scales, which are however under the resolution attained in numerical simulations. El-Kareh and Leal [15] have even raised the possibility that Oldroyd-like models may be ill-posed without the presence of non-local stress interactions, although this speculation has never been confirmed.

Our opinion is that in any case, a numerical method should not ignore the presence of a mechanism that creates sub-grid oscillations. Those oscillations destroy the smoothness which is implicitly assumed on the scale of a single computational

cell. Thus, truncation errors become dominant, and the response of the numerical method may become unpredictable. Note that it is not uncommon to have situations where sharp sub-grid variations occur, e.g., shock waves. Then, the numerical scheme has to be properly designed to account for the expected behavior of the sub-grid patterns. Shock waves are a classical example where naive discretization may lead to catastrophic breakdown.

A natural remedy in our case is to introduce stress diffusivity, with a diffusivity constant that depends on the mesh size, to damp out oscillations below the scale of the mesh. Such solution has been proposed in the past as a stabilizer, but has usually been avoided by the computational community. Indeed, computational rheologists have seen over the years numerous methods with good stability properties but poor accuracy, and the reluctance from corrections that smooth out sharp variations is understandable. An exception is turbulent flows, where sub-grid modelling is common practice even for Newtonian flows. Yet, we repeat, sub-grid oscillations cannot just be ignored. If local smoothing introduces large error, which means that those oscillations are dynamically important, then one has to resort to sub-grid modelling to account for the effects that sub-grid structures have on the large scale dynamics. We cannot determine at this point what is the correct approach. We believe that damping with a mesh-dependent coefficient may eliminate spurious patterns, and nevertheless converge with mesh refinement, but this belief has to be substantiated by numerical tests.

We conclude this section by raising a number of issues that remain open: (i) To what extent are our results generalizable to more general situations? The invariance of divergence-free stress fields is a special feature of Couette flow; in any other situation there is a non-trivial interaction between the stress and the velocity field. Yet, preliminary results indicate that divergence-free components in the stress field play an important role also in Poiseuille flow. It seems as if the same combination of transient growth and passive transport by shearing stream lines dominates numerical errors there too. (ii) In view of the new insight gained into the problem, the somewhat unexplained success of the DEVSSG schemes should be re-examined. It is of particular interest to determine whether their immunity to spurious instabilities results from an implicit insertion of cross-stream diffusion, or some other sort of regularization.

Acknowledgments

References

[1] V. Gorodsov, A. Leonov, On a linear instability of a plane parallel Couette flow of viscoelastic fluids, PPM 31 (1966) 289–299.
[2] M. Renardy, Y. Renardy, Linear stability of plane Couette flow of an upper convected Maxwell fluid, J. Non-Newton. Fluid Mech. 22 (1986) 23–33.
[3] R. Sureshkumar, A. Beris, Linear stability analysis of viscoelastic Poiseuille flow using an Arnoldi-based orthogonalization algorithm, J. Non-Newton. Fluid Mech. 56 (1995) 151–182.
[4] M. Graham, Effect of axial flow on viscoelastic Taylor–Couette instability, J. Fluid Mech. 360 (1998) 341–374.
[5] R. Sureshkumar, M. Smith, R. Armstrong, R. Brown, Linear stability and dynamics of viscoelastic flows using time dependent numerical simulations, J. Non-Newton. Fluid Mech. 82 (1999) 57–104.
[6] H. Wilson, M. Renardy, Y. Renardy, Structure of the spectrum in zero Reynolds number shear flow of the UCM and Oldroyd-B liquids, J. Non-Newton. Fluid Mech. 80 (1999) 251–268.
[7] M. Renardy, Location of the continuous spectrum in complex flows of the UCM fluid, J. Non-Newton. Fluid Mech. 94 (2000) 75–85.
[8] M. Renardy, A rigorous stability proof for plane Couette flow of an upper convected Maxwell fluid at zero Reynolds number, Eur. J. Mech. B 11 (1992) 511–516.
[9] R. Keiller, Numerical instability of time-dependent flows, J. Non-Newton. Fluid Mech. 43 (1992) 229–246.
[10] R. Brown, M. Szady, P. Northey, R. Armstrong, On the numerical stability of mixed finite-element methods for viscoelastic flows governed by differential constitutive equations, Theor. Comput. Fluid Dynam. 5 (1993) 77–106.
[11] M. Szady, T. Salamon, A. Liu, D. Bornside, R. Armstrong, R. Brown, A new mixed finite element method for viscoelastic flows governed by differential constitutive equations, J. Non-Newton. Fluid Mech. 59 (1995) 215–243.
[12] A. Bogaerds, G. Peters, F. Baaijens, Temporal stability of low-order continuous and discontinuous mixed finite element techniques for viscoelastic fluid mechanics, in: Proceedings of the XIIIth International Congress on Rheology, Cambridge, UK, 2000.
[13] A. Grillet, A. Bogaerds, G. Peters, F. Baaijens, Stability analysis of constitutive equations for polymer melts in viscometric flows, J. Non-Newton. Fluid Mech. 103 (2002) 221–250.
[14] M. Gerritsma, Time dependent numerical simulations of a viscoelastic fluid on a staggered grid, PhD Thesis, University of Gronigen, 1996.
[15] A. El-Kareh, L. Leal, Existence of solutions for all Deborah numbers for a non-Newtonian model midified to include diffusion, J. Non-Newton. Fluid Mech. 33 (1989) 257–287.
[16] R. Sureshkumar, A. Beris, Effect of artificial stress diffusivity on the stability of numerical calculations and the flow dynamics of time-dependent viscoelastic flows, J. Non-Newton. Fluid Mech. 60 (1995) 53–80.
[17] T. Vaithianathan, L. Collins, Numerical approach to simulating turbulent flow of a viscoelastic polymer solution, J. Comput. Phys. 187 (2003) 1–21.
[18] R. King, M. Apelian, R. Armstrong, R. Brown, Numerically stable finite element techniques for viscoelastic calculations in smooth and singular geometries, J. Non-Newton. Fluid Mech. 29 (1988) 147–216.

[19] I. Gel'fand, G. Shilov, Generalized Functions, Academic Press, New York, 1964.

[20] J. von Neumann, Mathematical Foundations of Quantum Mechanics, Princeton University Press, Princeton, NJ, 1955.

[21] M. Abramowitz, I. Stegun, Handbook of Mathematical Functions with Formulas, Graphs, and Mathematical Tables, Dover, New York, 1971.

[22] F. Harlow, J. Welch, Numerical calculation of time-dependent viscous incompressible flow of fluid with a free surface, Phys. Fluids 8 (1965) 2182.

[23] L. Trefethen, Pseudospectra of linear operators, SIAM Rev. 39 (1997) 383–406.

[24] A. Trefethen, N. Trefethen, P. Schmid, Spectra and pseudospectra for pipe Poiseuille flow, Comput. Meth. Appl. Mech. Eng. 175 (1999) 413–420.

[25] S. Orszag, A. Patera, Secondary instability of wall-bounded shear flows, J. Fluid Mech. 128 (1983) 347–385.

[26] K. Atalik, R. Keunings, Non-linear temporal stability analysis of viscoelastic channel flows using a fully spectral method, J. Non-Newton. Fluid Mech. 102 (2002) 299–319.

[27] T. Write, Eigtool, a graphical tool for nonsymmetric eigenproblems. http://web.comlab.ox.ac.uk/projects/pseudospectra/eigtool/.

[28] M. Embree, L. Trefethen, Generalizing eigenvalue theorems to pseudospectra theorems, SIAM J. Sci. Comput. 23 583–590.